A THESIS

FOR THE DEGREE OF MASTER OF SCIENCE

Unit Cells for Filter Design Based on CPW Metamaterial Transmission Line

Lei Yang

Department of Telecommunication Engineering

GRADUATE SCHOOL

JEJU NATIONAL UNIVERSITY

JUNE 2013

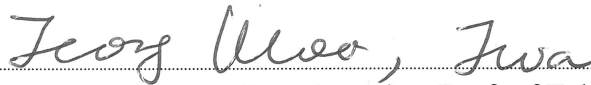# Unit Cells for Filter Design Based on CPW Metamaterial Transmission Line

Lei Yang

(Supervised by Professor Doo-Yeong Yang)

A thesis submitted in partial fulfillment of the requirement for the
degree of Master of Science

2013. 06

The thesis has been examined and approved.

Jeong Woo, Jwa
....
Thesis director, Jeong-Woo Jwa, Associate Prof. of Telecommunication Engineering

....
Seung-Yeup Hyun, Assistant Prof. of Telecommunication Engineering

....
Doo-Yeong Yang, Prof. of Telecommunication Engineering

2013. 6. 3
Date

Department of Telecommunication Engineering

GRADUATE SCHOOL

JEJU NATIONAL UNIVERSITY

REPUBLIC OF KOREA

To

My Family

Acknowledgements

I would like to thank everyone who has helped me during my study.

First of all, I would like to thank my supervisor, Prof. Doo-Yeong Yang, for his tender guidance and endless support. Prof. Yang is a sympathetic and principle-centered person. His enthusiasm and unique view on research have made a deep impression on me. Under his guidance, I become more motivated and knowledgeable.

Secondly, I would like to express my sincere appreciation to the members of my committee, Prof. Jeong-Woo Jwa and Prof. Seung-Yeup Hyun, who monitored my work and took effort in reading and providing me with valuable comments on my thesis.

Moreover, I wish to offer my humble gratitude to the professors in my department, Prof. Heung-Soo Kim, Prof. Jea-Yun Lim, Prof. Jin-Shig Kang, and Prof. Soon-Whan Kim, for their inspiring and encouraging way to guide me to a deeper understanding of knowledge, and their invaluable comments during the course work.

I am also grateful for the department of Telecommunication Engineering at Jeju National University for providing me an excellent work environment during my study and I would like to thank Eun-Jeong Hyun and Ji-Yoon Kim for their cheerful assistance.

Additionally, I would like to thank the Innertron Inc. for providing me technical and financial supports, as well as helpful assistance.

Finally, I will never find words enough to express the gratitude that I owe to my family. Their tender love and affection have always been the cementing force for building the blocks of my study.

Abstract

In the recent, metamaterials (MTMs) have concentrated extensive attention in many areas. This artificial material has simultaneously negative permittivity and permeability. Therefore, MTMs have special characteristics not occur in conventional materials. And the targets of miniaturization and low power loss can be possible if MTMs are used in microwave component or system design.

In this thesis, the concepts and the fundamental properties of MTMs were illustrated. And several unit cells for filter design based on coplanar waveguide (CPW) MTM transmission line were proposed. First of all, a left-handed (LH) unit cell and a dual left-handed (DLH) unit cell with high-pass property were devised by the conventional composite right and left-handed (C-CRLH) theory based on folded coplanar waveguide (FCPW). Secondly, a right-handed (RH) unit cell with low-pass property was devised by the C-CRLH theory based on conductor-backed coplanar waveguide (CBCPW). Moreover, a unit cell with a conductor-backed defected ground (CBDG) structure based on dual composite right and left-handed (D-CRLH) CBCPW, and a unit cell with a groove line (GL) structure based on D-CRLH CPW showed band-rejection property.

The characteristics of the proposed unit cells were analyzed by using high frequency structural simulator. By tuning the sizes of the unit cells, the parameters of the RH and LH immittance components were optimized and the desired characteristics of the unit cells were achieved. In addition, the equivalent circuits for the unit cells were extracted and analyzed by employing advanced design system. As a result, the S-parameter simulation results of the unit cells showed good agreements with those of the equivalent circuits. On the other hand, the dispersion characteristics and the energy distributions of the electromagnetic field were simulated to confirm the characteristics of C-CRLH and D-CRLH structures. These simulation results provided the design data of the proposed structures. Through the photosensitizing,

etching, plating and assembling processes, the proposed unit cells were fabricated on the substrates made by Taconic with the relative dielectric constant of 2.5 and the substrate thickness of 0.787mm. And then, the fabricated unit cells were measured by the vector network analyzer of N5230A.

As a result, the LH unit cell based on C-CRLH FCPW exhibited high-pass property with -9.88dB rejection in the range beyond 2.05GHz. And the DLH unit cell based on C-CRLH FCPW showed high-pass property that the return loss is more than 10dB in the range of 2.52 ~ 2.9GHz and the range beyond 4.23GHGHz of the pass-band. On the other hand, the RH unit cell based on C-CRLH CBCPW exhibited low-pass property with -16dB rejection and a 0.38dB insertion loss in the pass-band and a good skirt effect. Moreover, the CBDG unit cell based on D-CRLH CBCPW with band-rejection property showed a 0.6dB return loss and a 16dB insertion loss from 869MHz to 894MHz of the stop-band. And the GL unit cell based on D-CRLH CPW exhibited band-rejection property with an 11dB insertion loss and a 2dB return loss in the stop-band from 869MHz to 894MHz.

In practical applications, since the proposed unit cells have good characteristics with compact structures, they can be used not only in filter design but also in other components of microwave systems, such as couplers and resonators. Especially, the compact unit cells are very useful for the designs of dual-band or multi-band duplexers, which have operational frequencies separated and combined by various frequency bands.

Contents

List of Figures

List of Tables

Glossary of Acronyms and Abbreviations

ADS	Advanced Design System
BPF	Band-Pass Filter
BRF	Band-Rejection Filter
CBCPW	Conductor-Backed Coplanar Waveguide
CBDG	Conductor-Backed Defected Ground
C-CRLH	Conventional Composite Right and Left-Handed
CPW	Coplanar Waveguide
CRLH	Composite Right and Left-Handed
DC	Direct Current
D-CRLH	Dual Composite Right and Left-Handed
DLH	Dual Left-Handed
FCPW	Folded Coplanar Waveguide
GL	Groove Line
HFSS	High Frequency Structural Simulator
HPF	High-Pass Filter
LH	Left-Handed
LHM	Left-Handed Material
LPF	Low-Pass Filter
MIC	Microwave Integrated Circuit
MMIC	Monolithic Microwave Integrated Circuit
MTM	Metamaterial
PCB	Printed Circuit Board
PLH	Purely Left-Handed
PRH	Purely Right-Handed
RCP	Rectangular Conductor Patch
RGP	Rectangular Grounded Patch

RH	Right-Handed
SRR	Split-Ring Resonator
TEM	Transverse Electromagnetic Mode
TL	Transmission Line
TW	Thin-Wire

Chapter 1   Introduction

Recently, metamaterial (MTM) has concentrated extensive attention in many areas. This artificial MTM with simultaneously negative permittivity (ε) and permeability (μ), more commonly referred to as left-handed material (LHM), was presented in 1967 by the Russian physicist Viktor Veselago and several fundamental phenomena occurring in MTM were predicted by Veselago [1]:

1. The phenomenon of backward wave with antiparallel group and phase velocities referring to as left-handed (LH).
2. Reversal of Snell's law.
3. Reversal of Doppler effect.
4. The nonlinear characteristics because of frequency dispersion.

After that, the first LHM was demonstrated experimentally in 2000 by a group at the University of California, San Diego [2]. They combined a thin-wire (TW) and a split-ring resonator (SRR) structures into a LH structure. However, the TW-SRR LHM is not suitable for microwave applications because the structure is resonant and consequently exhibits high loss and narrow bandwidth. Thus, a transmission line (TL) approach of LHM was introduced in 2002 [3]-[4]. Since LHM is actually a homogeneous structure, the artificial LH TL can be constructed effectively. The advantages of LH TL are high frequency selectivity, low loss and wide bandwidth, as well as it can be implemented in planar configurations, compatible with modern microwave integrated circuits (MICs) [5]. Therefore, LH TL can be widely used for the efficient designs of microwave applications, in order to get the targets of miniaturization, low cost and low power loss. But a purely left-handed (PLH) structure does not exist in fact because the parasitic elements exist, and that was the motivation for the introduction of the term "composite right and left-handed (CRLH)". A CRLH model has a LH range, which is due to the effect of the loading elements, and a right-handed (RH) range, which is due to the parasitic elements of the TL [5]-[6].

An effectively homogeneous CRLH TL can be constructed by cascading LC-based unit cells in either a non-periodic or periodic fashion. The LC-based unit cell for a conventional composite right and left-handed (C-CRLH) TL consists of an impedance constituted by a RH inductance in series with a LH capacitance and an admittance constituted by a RH capacitance in parallel with a LH inductance. On the other hand, the unit cell for a dual composite right and left-handed (D-CRLH) TL consists of an impedance constituted by a RH inductance in parallel with a LH capacitance and an admittance constituted by a RH capacitance in series with a LH inductance [15]. Since the structures of the LC-based unit cells are similar to conventional filters, low-pass filter (LPF), high-pass filter (HPF), band-pass filter (BPF) and band-rejection filter (BRF) can be designed by tuning to the RH and LH contributions on the CRLH TLs, which are composed of cascading LC-based unit cells [7]-[9].

Filters are essential components in precision measuring instruments, which are commonly used in testing RF communication products. The development of the precision measuring instruments requires filters to have a compact structure and low insertion loss. Among the ways of configuring filters, which are used in high precision measuring instruments without high power, a quarter wavelength microstrip line is commonly used. However, filters designed by meta-unit cell, which is basically one eighth wavelength, can be smaller in size and the insertion loss can be decreased. In the respect of designing filters in MICs or monolithic microwave integrated circuits (MMICs), coplanar waveguide (CPW) is more suitable because of its advantages, such as the simplicity of fabrication, easy mounting of active and passive devices in series and shunt, easy connections without via hole and possible size reduction [10]-[12]. Conductor-backed coplanar waveguide (CBCPW) is similar to conventional CPW, but it has an additional bottom layer ground plane. The bottom layer ground plane of CBCPW increases mechanical strength of the circuit and gets cooling effect for the circuit with active devices. Moreover, CBCPW gets less dispersive than CPW [10], [14].

In this thesis, unit cells are proposed based on CPW MTM TL for designing the filters used in precision measuring instruments. And the equivalent circuits for the proposed unit cells are extracted to analyze the performances. Also, the dispersion

characteristics and the energy distributions of the electromagnetic field are simulated to prove the properties of C-CRLH and D-CRLH structures. In the end, the unit cells are fabricated and *S*-parameter characteristics are measured.

This thesis is organized as follows: Chapter 2 illustrates the theoretical backgrounds of MTM and the C-CRLH and D-CRLH MTM TL theories. In addition, the basic characteristics of CPW and CBCPW are introduced. In Chapter 3, unit cells with high-pass property and low-pass property are proposed based on C-CRLH CPW. In Chapter 4, unit cells with band-rejection property are implemented based on D-CRLH CPW. Finally, Chapter 5 summarizes this thesis.

Chapter 2   Theoretical Backgrounds

2.1 Backgrounds of MTMs

MTMs are broadly defined as effectively homogeneous structures with special electromagnetic properties not practically available in nature. Since the structural average cell size of an effectively homogeneous structure is much smaller than the guided wavelength, the structure can be regarded as the effectively homogeneous structure when its average cell size is less than a quarter of the wavelength. In medium with effective-homogeneity, the refractive index n can be calculated by the permittivity ε and the permeability μ as follows:

$$n = \pm\sqrt{\varepsilon\mu}. \tag{2-1}$$

Depending on the signs of ε and μ, four possible combinations in the pair (ε, μ) are available, as shown in Figure 2.1. The I, II and IV quadrants of Figure 2.1 are well known in conventional materials, but the III quadrant, with simultaneously negative ε and μ, corresponds to the new class of LHMs [1]-[2], [5].
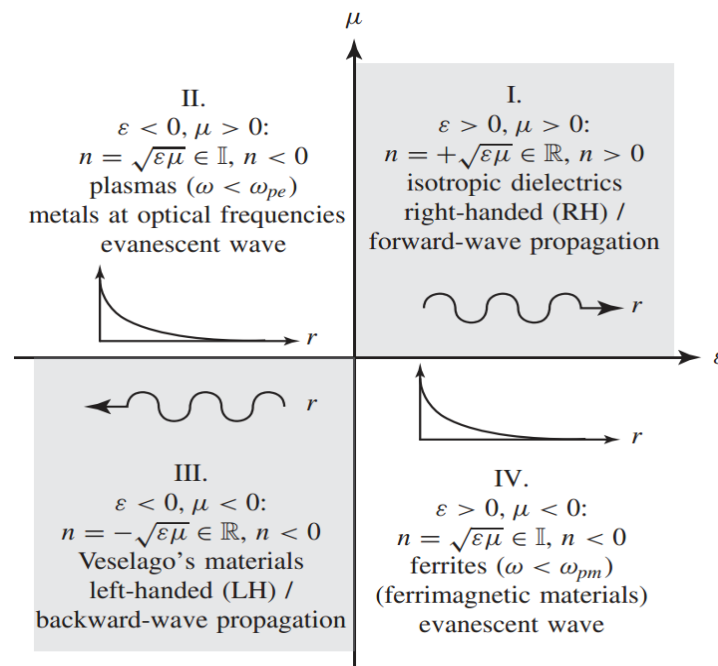
Figure 2.1 Permittivity-permeability (ε - μ) and refractive index (n) diagram of materials.

In LHMs, the phase velocity and the group velocity are antiparallel and the refraction index has a negative value. In order to understand the differences of fundamental phenomena between a LH medium and a common RH medium, Maxwell's equations are considered. Assuming fields vary sinusoidally with time at radian frequency and defining the time-harmonic fields as

$$\overline{E} = \text{Re}\left(\overline{E}e^{j\omega t}\right), \tag{2-2a}$$

$$\overline{H} = \text{Re}\left(\overline{H}e^{j\omega t}\right). \tag{2-2b}$$

Then Maxwell's equations can be written as

$$\nabla \times \overline{E} = -j\omega\mu\overline{H} - \overline{M}_s, \tag{2-3a}$$

$$\nabla \times \overline{H} = j\omega\varepsilon\overline{E} + \overline{J}_s, \tag{2-3b}$$

$$\nabla \bullet \overline{D} = \rho_e, \tag{2-3c}$$

$$\nabla \bullet \overline{B} = \rho_m. \tag{2-3d}$$

Consider the plane waves in a lossless medium without sources ($\overline{M}_s = \overline{J}_s = 0$), the equations of the electromagnetic field can be written as

$$\overline{E} = \overline{E}_0 e^{-j\beta r}, \tag{2-4a}$$

$$\overline{H} = \frac{\overline{E}_0}{\eta} e^{-j\beta r}, \tag{2-4b}$$

and substitute them into Equations (2-3a) and (2-3b). Then, the simplified equations are

$$\overline{\beta} \times \overline{E} = s\omega|\mu|\overline{H}, \tag{2-5a}$$

$$\overline{\beta} \times \overline{H} = -s\omega|\varepsilon|\overline{E}, \tag{2-5b}$$

$$\beta = n\frac{\omega}{c}, \tag{2-5c}$$

where

> s=+1   in a RH medium,
> s=-1   in a LH medium.

5

Since the Poynting vector is defined as

$$\overline{S} = \overline{E} \times \overline{H^*},$$ (2-6)

the triad of the electric field, the magnetic field, the wave vector and the Poynting vector in a medium can be built as Figure 2.2. In Figure 2.2, the direction of the Poynting vector $\overline{S}$, which can be considered as the direction of power flow over time, is oriented towards the same direction of propagation of energy and parallel to the group velocity v_g ($v_g = \partial\omega/\partial\beta$). However, the phase velocity v_p, corresponds to the propagation of a perturbation, is dependent on the constitution parameters (ε and μ) of the medium,

$$v_p = \frac{1}{\sqrt{\mu\varepsilon}} = \frac{\omega}{\beta},$$ (2-7)

where

RH medium: $v_p > 0$,

LH medium: $v_p < 0$.

As a result, the group velocity v_g and the phase velocity v_p of electromagnetic waves in a LH medium are antiparallel, known as backward waves [2], [5].
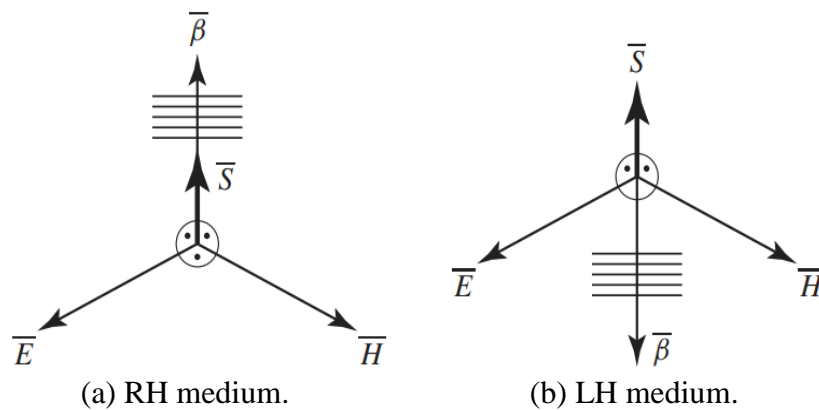
(a) RH medium.   (b) LH medium.
Figure 2.2 Electric field, magnetic field, wave vector and Poynting vector for an electromagnetic wave in a medium.

2.2 C-CRLH MTM TL Theory

The TL approach for LHM is based on the dual configuration of a conventional RH TL. The equivalent circuit for a lossless purely right-handed (PRH) TL consists of a per-unit-length series inductance $L_R^{'c}$ (H/m) and a per-unit-length shunt capacitance $C_R^{'c}$ (F/m), as shown in Figure 2.3(a). And the equivalent circuit for a lossless PLH TL is dual to the equivalent circuit for the lossless PRH TL, which has a times-unit-length series capacitance $C_L^{'c}$ (F·m) and a times-unit-length shunt inductance $L_L^{'c}$ (H·m), as shown in Figure 2.3(b). However, due to the nature of a TL of parasitic series inductance and shunt capacitance, the PLH TL does not exist. Therefore, a C-CRLH TL combining the PLH TL with the PRH TL is formed [6]. As shown in Figure 2.3(c), the equivalent circuit for a lossless C-CRLH TL consists of a RH per-unit-length inductance $L_R^{'c}$ (H/m) in series with a LH times-unit-length capacitance $C_L^{'c}$ (F·m) and a RH per-unit-length capacitance $C_R^{'c}$ (F/m) in parallel with a LH times-unit-length inductance $L_L^{'c}$ (H·m). Consequently, the per-unit-length impedance is

$$Z_c^{'} = j\left(\omega L_R^{'c} - \frac{1}{\omega C_L^{'c}} \right), \tag{2-8}$$

and the per-unit-length admittance is

$$Y_c^{'} = j\left(\omega C_R^{'c} - \frac{1}{\omega L_L^{'c}} \right). \tag{2-9}$$

Then the characteristic impedance can be calculated as follows:

$$Z_0^c = \sqrt{\frac{Z_c^{'}}{Y_c^{'}}} = \sqrt{\frac{j\left(\omega L_R^{'c} - \frac{1}{\omega C_L^{'c}} \right)}{j\left(\omega C_R^{'c} - \frac{1}{\omega L_L^{'c}} \right)}}. \tag{2-10}$$

At low frequency ($\omega \rightarrow 0$), the values of RH series inductance ($L_R^{'c}$) and shunt capacitance ($C_R^{'c}$) get very smaller and the LH components ($C_L^{'c}$ and $L_L^{'c}$) are left only. So that the C-CRLH TL becomes equivalent to the PLH TL and the PLH TL is of high-pass nature. The PLH characteristic impedance is

제주대학교 중앙도서관
JEJU NATIONAL UNIVERSITY LIBRARY

$$Z_0^c = Z_L^c = \sqrt{\frac{L_L^{'c}}{C_L^{'c}}}. \tag{2-11}$$

On the contrary, at high frequency ($\omega \to \infty$), the values of LH series capacitance ($C_L^{'c}$) and shunt inductance ($L_L^{'c}$) get close to zero and the RH components ($L_R^{'c}$ and $C_R^{'c}$) are left only. So the C-CRLH TL becomes equivalent to the PRH TL and the PRH TL is of low-pass nature. The PRH characteristic impedance is

$$Z_0^c = Z_R^c = \sqrt{\frac{L_R^{'c}}{C_R^{'c}}}. \tag{2-12}$$

In the entire frequency band, the C-CRLH TL shows band-pass or band-stop nature depending on the characteristics of the RH and LH TLs. The characteristic impedance becomes

$$Z_0^c = \sqrt{\frac{Z_c^{'}}{Y_c^{'}}} = Z_L^c \sqrt{\frac{\left(\omega / \omega_{se}^c\right)^2 - 1}{\left(\omega / \omega_{sh}^c\right)^2 - 1}}, \tag{2-13}$$

(a) Equivalent circuit for a lossless
PRH TL.

(b) Equivalent circuit for a lossless
PLH TL.
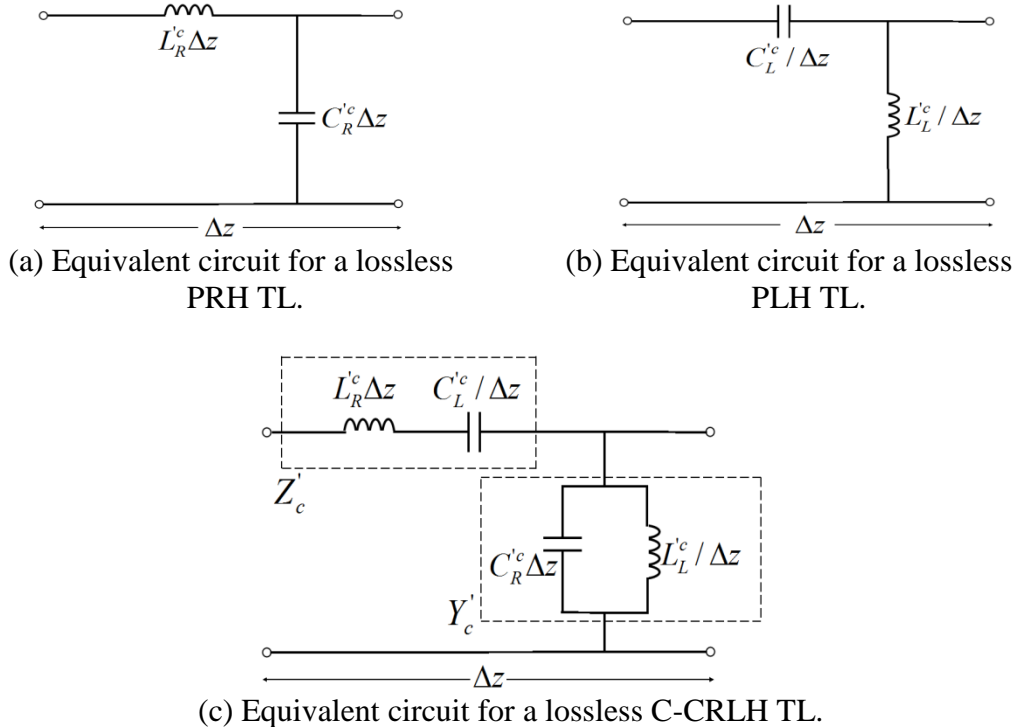
(c) Equivalent circuit for a lossless C-CRLH TL.
Figure 2.3 Equivalent circuits for lossless PRH, PLH and C-CRLH TLs.

where

$$\omega_{se}^c = \frac{1}{\sqrt{L_R^{'c}C_L^{'c}}}, \tag{2-14a}$$

$$\omega_{sh}^c = \frac{1}{\sqrt{L_L^{'c}C_R^{'c}}}. \tag{2-14b}$$

And the complex propagation constant of the C-CRLH TL can be calculated as follows:

$$\gamma_c = \alpha_c + j\beta_c = js(\omega)\sqrt{\left(\frac{\omega}{\omega_R^c}\right)^2 + \left(\frac{\omega_L^c}{\omega}\right)^2 - k_c\omega_L^{c2}}, \tag{2-15}$$

where

$$s(\omega) = \begin{cases} -1, & if \quad \omega < \omega_{\Gamma 1} = \min\left(\omega_{se}^c, \omega_{sh}^c\right) \\ +1, & if \quad \omega > \omega_{\Gamma 2} = \max\left(\omega_{se}^c, \omega_{sh}^c\right) \end{cases}, \tag{2-16}$$

and the variables are

$$\omega_R^c = \frac{1}{\sqrt{L_R^{'c}C_R^{'c}}}, \tag{2-17a}$$

$$\omega_L^c = \frac{1}{\sqrt{L_L^{'c}C_L^{'c}}}, \tag{2-17b}$$

$$k_c = L_R^{'c}C_L^{'c} + L_L^{'c}C_R^{'c}. \tag{2-17c}$$

As shown in Equation (2-15), the propagation constant can be purely imaginary ($\gamma_c = j\beta_c$) and a pass-band exists. On the other hand, the propagation constant can be purely real ($\gamma_c = \alpha_c$) and a stop-band occurs. The stop-band is the unique characteristic of the C-CRLH TL, but does not exist in the case of the PRH TL or the PLH TL.

Figure 2.4 shows the dispersion characteristics of the PRH, PLH and C-CRLH TLs in accordance with the frequency and the phase constant. And the group velocity and the phase velocity can be inferred by Figure 2.4. Figure 2.4(a) shows the characteristic curve of the PRH TL, which is situated on the right side of the zero point. That is, the phase constant is positive ($\beta_R^c = \omega\sqrt{C_R^{'c}L_R^{'c}}$). At the same time, the group velocity and the phase velocity have the same sign ($v_g v_p > 0$). On the other

9

hand, the curve of the PLH TL is placed on the left of the zero point while the phase constant is negative ($\beta_L^c = -1/\omega\sqrt{C_L'^c L_L'^c}$) and the group and phase velocities are antiparallel ($v_g v_p < 0$).

As shown in Figure 2.4(c), the C-CRLH TL has both RH and LH bands. When the series resonant frequency (ω_{se}^c) and the shunt resonant frequency (ω_{sh}^c) are not the same, there is a gap between the RH band and the LH band. In this case, the C-CRLH TL is said to be unbalanced. When the series resonant frequency and the shunt resonant frequency are the same ($\omega_{se}^c = \omega_{sh}^c$), the gap closes up with nonzero group velocity and the C-CRLH TL is said to be balanced, as shown in Figure 2.5. In this case, the phase constant is the sum of the phase constants of PRH and PLH TLs ($\beta_c = \beta_R^c + \beta_L^c = \omega\sqrt{C_R'^c L_R'^c} - 1/\omega\sqrt{C_L'^c L_L'^c}$).

As mentioned above, the C-CRLH TL shows LH characteristic at low frequencies and RH characteristic at high frequencies. And the transition frequency between the RH band and the LH band is

(a) PRH property.   (b) PLH property.
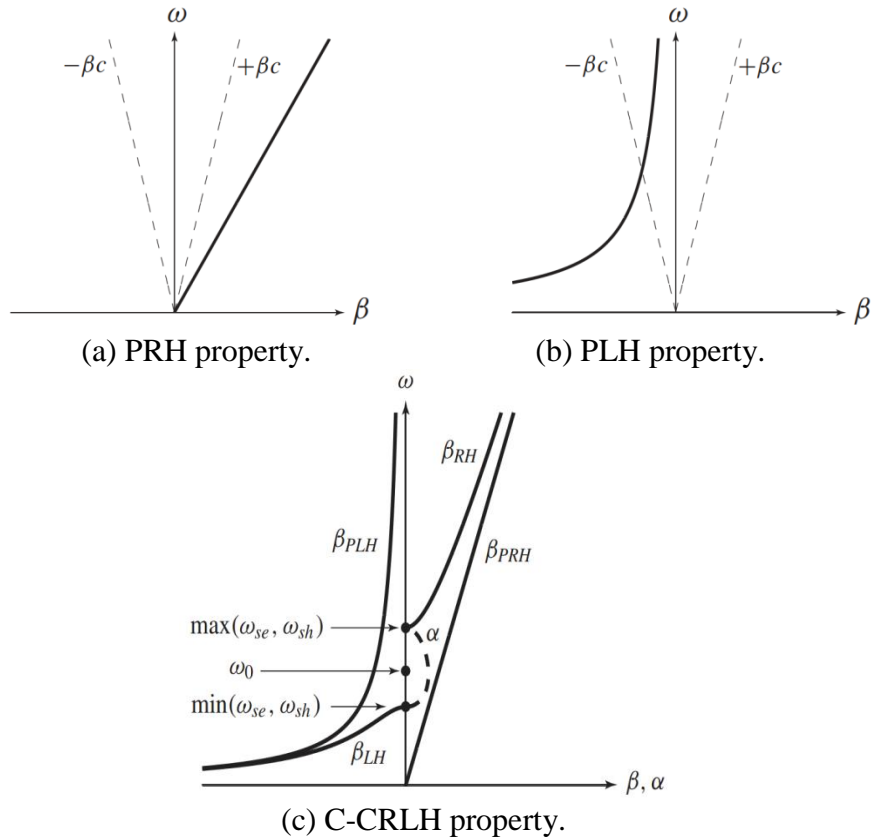
(c) C-CRLH property.
Figure 2.4 Dispersion characteristics of PRH, PLH and C-CRLH TLs.

$$\omega_0^c = \frac{1}{\sqrt[4]{L_R^{'c} C_R^{'c} L_L^{'c} C_L^{'c}}}. \tag{2-18}$$

In the case of a balanced C-CRLH TL, the dispersion curve appears smooth and the stop-band does not exist. The phase constant is 0 at ω_0^c and the phase shift of the TL with length d is 0 ($\varphi = -\beta d = 0$). And the phase is advance ($\varphi > 0$) in the LH band ($\omega < \omega_0^c$) and delay ($\varphi < 0$) in the RH band ($\omega > \omega_0^c$). Then the characteristic impedance of the balanced C-CRLH TL is

$$Z_0^c = Z_L^c = Z_R^c. \tag{2-19}$$

As shown in Equation (2-19), the characteristic impedance of the balanced C-CRLH TL is independent of frequency and it allows for broadband matching.

Assuming that the electromagnetic waves transmit in a transverse electromagnetic mode (TEM) in the MTM, the electrical parameters ($L_R^{'c}$, $C_R^{'c}$, $L_L^{'c}$, $C_L^{'c}$) representing the characteristics of the C-CRLH TL can be associated with the constitutive parameters (ε and μ). The phase constant of the lossless C-CRLH TL is $\beta_c = \sqrt{Z_c' Y_c'}$ and the phase constant of a material is $\beta_c = \omega\sqrt{\mu\varepsilon}$. Then the relation can be set up as follows:

$$-\omega^2 \mu\varepsilon = Z_c' Y_c'. \tag{2-20}$$

Similarly, the characteristic impedance of the C-CRLH TL ($Z_0^c = \sqrt{Z_c'/Y_c'}$) can be associated with the inherent impedance of a material ($\eta = \sqrt{\mu/\varepsilon}$) as follows:

$$\frac{Z_c'}{Y_c'} = \frac{\mu}{\varepsilon}. \tag{2-21}$$

(a) Equivalent circuit. (b) Dispersion curve.
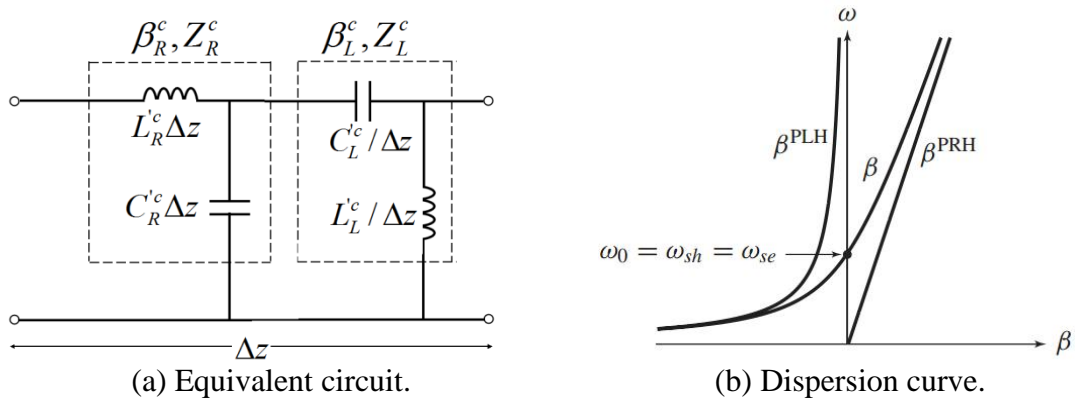
Figure 2.5 Characteristics of a lossless balanced C-CRLH TL.

11

Thus, the relationship between the electrical parameters and the constitutive parameters can be calculated by Equations (2-8), (2-9), (2-20) and (2-21) as follows:

$$\mu = \frac{Z_c^{'}}{j\omega} = L_R^{'c} - \frac{1}{\omega^2 C_L^{'c}}, \qquad (2\text{-}22a)$$

$$\varepsilon = \frac{Y_c^{'}}{j\omega} = C_R^{'c} - \frac{1}{\omega^2 L_L^{'c}}. \qquad (2\text{-}22b)$$

At the lowest frequency, the equivalent parameters are equal to the dispersive parameters of the PLH TL ($\mu(\omega \to 0) = -1\big/\big(\omega^2 C_L^{'c}\big)$ and $\varepsilon(\omega \to 0) = -1\big/\big(\omega^2 L_L^{'c}\big)$). And at the highest frequency, the equivalent parameters are equal to the non-dispersive parameters of the PRH TL ($\mu(\omega \to \infty) = L_R^{'c}$ and $\varepsilon(\omega \to \infty) = C_R^{'c}$). In addition, the refractive index ($n = c\beta_c / \omega$) plot for the balanced and unbalanced C-CRLH TLs is shown in Figure 2.6, which shows a negative refractive index in the LH band and positive in the RH band.

A homogeneous C-CRLH TL does not exist in nature, but an effectively homogeneous C-CRLH TL can be manufactured in the conditions of continuity of electromagnetic waves since the guided wavelength is much longer than the length of TL within a certain frequency range. The effectively homogeneous C-CRLH TL of length d can be constructed by cascading the LC-based unit cell of Figure 2.7(a) in periodic or non-periodic. The unit cell consists of an impedance Z_c (Ω) constituted by a RH inductance L_R^c (H) in series with a LH capacitance C_L^c (F) and an admittance Y_c (S) constituted by a RH capacitance C_R^c (F) in parallel with a LH inductance L_L^c (H).
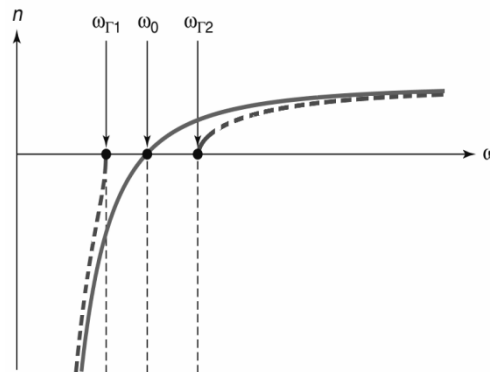
Figure 2.6 Refractive index plots for balanced (solid line) and unbalanced (dotted line) C-CRLH TLs.

12

The unit cell in Figure 2.7(a) is non-dimensional unit cell, which is unlike the unit cell with physical lengths in Figure 2.3(c). The phase of the LC-based unit cell can be interpreted from the viewpoint of the electrical length ($\theta = \Delta\varphi(rad)$). However, the physical length p is determined by the inductors and capacitors used in implementation. In the limit $p = \Delta z \to 0$, the LC-based unit cell of Figure 2.7(a) is equivalent to the incremental model of Figure 2.3(c). Therefore, an ideal homogeneous lossless C-CRLH TL of length d can be configured by cascading the LC-based unit cell which satisfies the condition $p \to 0$, as shown in Figure 2.7(b). In practice, if the unit cell is smaller than a quarter of the guided wavelength, the electrical length of the unit cell is smaller than $\pi/2$ and the LC-based C-CRLH TL can be seen as an effectively homogeneous structure by electromagnetic waves.

By applying the periodic boundary conditions related to the Bloch-Floquet theory to the LC-based unit cell, the phase constant can be calculated as

$$\beta_c = \frac{1}{p}\cos^{-1}\left(1 + \frac{Z_c Y_c}{2}\right), \tag{2-23}$$

where the series impedance and the shunt admittance of the LC-based unit cell are given by

$$Z_c = j\left(\omega L_R^c - 1/\omega C_L^c\right), \tag{2-24a}$$

$$Y_c = j\left(\omega C_R^c - 1/\omega L_L^c\right), \tag{2-24b}$$

with $L_R^c = L_R^{'c}\Delta z$, $C_R^c = C_R^{'c}\Delta z$, $L_L^c = L_L^{'c}/\Delta z$ and $C_L^c = C_L^{'c}/\Delta z$.

Since the electrical length of the unit cell is small, the phase constant can be calculated by applying the Taylor approximation ($\cos(\beta_c p) \approx 1 - (\beta_c p)^2/2$) as follows:

$$\beta_c = \frac{s(\omega)}{p}\sqrt{\left(\omega L_R^c - \frac{1}{\omega C_L^c}\right)\left(\omega C_R^c - \frac{1}{\omega L_L^c}\right)}. \tag{2-25}$$

And the dispersion characteristics of the balanced and unbalanced LC-based C-CRLH TLs are shown in Figure 2.8.

(a) Unit cell.
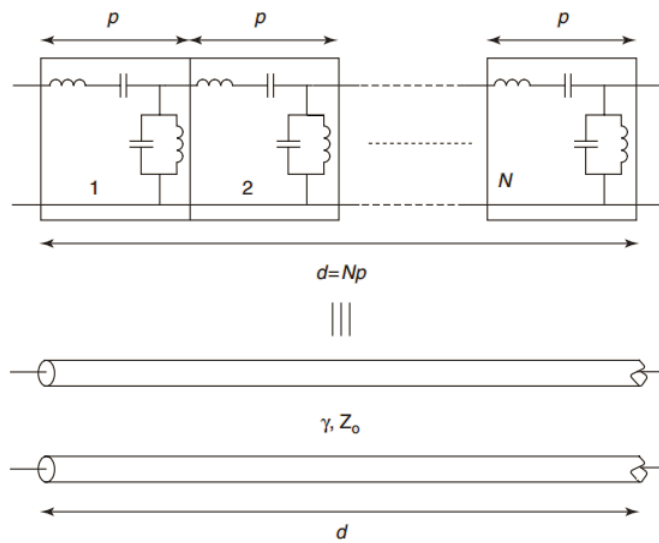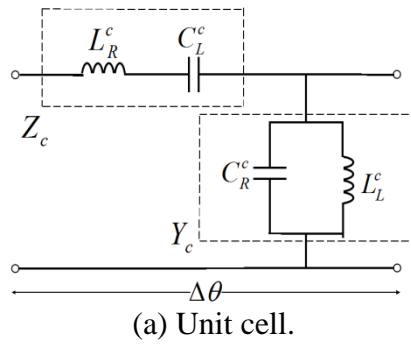
(b) LC periodic network equivalent to a homogeneous lossless C-CRLH of length d for $p{\to}0$.

Figure 2.7 Equivalent models for an LC-based C-CRLH TL.
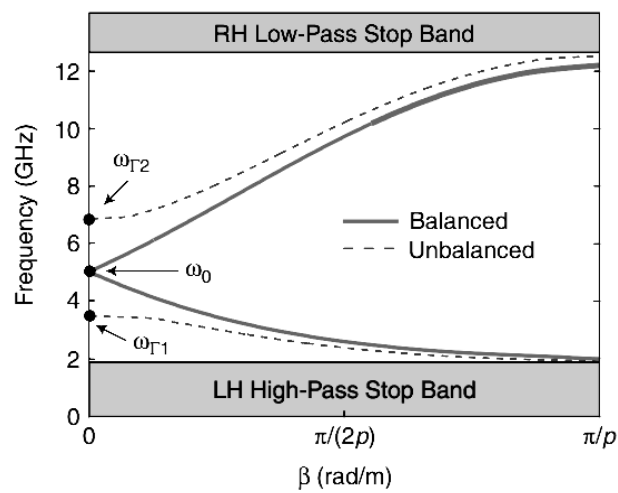
Figure 2.8 Dispersion characteristics of an LC-based C-CRLH TL.

2.3 D-CRLH MTM TL Theory

The equivalent circuit for a homogeneous lossless D-CRLH TL [15] is shown in Figure 2.9. It consists of a RH per-unit-length inductance $L_R^{'d}$ (H/m) in parallel with a LH times-unit-length capacitance $C_L^{'d}$ (F·m) and a RH per-unit-length capacitance $C_R^{'d}$ (F/m) in series with a LH times-unit-length inductance $L_L^{'d}$ (H·m). Consequently, the per-unit-length impedance is

$$Z_d^{'} = j\frac{\omega L_R^{'d}}{1-\left(\omega/\omega_{se}^d\right)^2},$$ (2-26)

and the per-unit-length admittance is

$$Y_d^{'} = j\frac{\omega C_R^{'d}}{1-\left(\omega/\omega_{sh}^d\right)^2},$$ (2-27)

where

$$\omega_{se}^d = \frac{1}{\sqrt{L_R^{'d}C_L^{'d}}},$$ (2-28a)

$$\omega_{sh}^d = \frac{1}{\sqrt{L_L^{'d}C_R^{'d}}}.$$ (2-28b)

Then the characteristic impedance and the propagation constant can be calculated as follows:

$$Z_0^d = Z_{0r}^d + jZ_{0i}^d = \sqrt{\frac{Z_d^{'}}{Y_d^{'}}} = Z_R^{'d}\sqrt{\frac{1-\left(\omega/\omega_{sh}^d\right)^2}{1-\left(\omega/\omega_{se}^d\right)^2}},$$ (2-29a)

$$\gamma_d = \alpha_d + j\beta_d = \sqrt{Z_d^{'}Y_d^{'}} = \frac{js(\omega)\omega\omega_L^{'d}}{\sqrt{\omega^4-\left(\omega_{se}^{d2}+\omega_{sh}^{d2}\right)\omega^2+\omega_{se}^{d2}\omega_{sh}^{d2}}},$$ (2-29b)
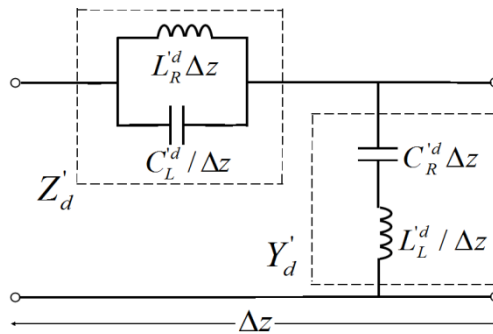
Figure 2.9 Equivalent circuit for a homogeneous lossless D-CRLH TL.

15

where

$$Z_R^{'d} = j\omega L_R^{'d}, \tag{2-30a}$$

$$\omega_L^{'d} = \frac{1}{\sqrt{L_L^{'d} C_L^{'d}}}, \tag{2-30b}$$

$$s(\omega) = \begin{cases} +1, & if \quad \omega < \omega_{\Gamma 1} = \min\left(\omega_{se}^d, \omega_{sh}^d\right) \\ -1, & if \quad \omega > \omega_{\Gamma 2} = \max\left(\omega_{se}^d, \omega_{sh}^d\right) \end{cases}. \tag{2-30c}$$

The characteristics of the homogeneous D-CRLH TL is determined by the impedances ($Z_R^{'d}$ and $Z_L^{'d} = 1/j\omega C_L^{'d}$) and the admittances ($Y_R^{'d} = j\omega C_R^{'d}$ and $Y_L^{'d} = 1/j\omega L_L^{'d}$). At low frequencies, the components L_R^d and C_R^d determine the characteristic of the TL since $Z_R^{'d} \ll Z_L^{'d}$ and $Y_R^{'d} \ll Y_L^{'d}$. In this case, the D-CRLH TL shows RH characteristic. At high frequencies, the components $L_L^{'d}$ and $C_L^{'d}$ determine the characteristic since $Z_R^{'d} \gg Z_L^{'d}$ and $Y_R^{'d} \gg Y_L^{'d}$. In this case, the D-CRLH shows LH characteristic. Therefore, the characteristic of the D-CRLH TL is opposite to the C-CRLH TL, which is band-rejection in nature.

When the D-CRLH TL is balanced ($\omega_{se}^d = \omega_{sh}^d = \omega_0^d$ or $L_R^{'d} C_L^{'d} = L_L^{'d} C_R^{'d}$), the characteristic impedance and the propagation constant can be simplified as follows:

$$Z_{0r}^d = Z_R^{'d}(const.), \quad Z_{0i}^d = 0, \tag{2-31a}$$

$$\beta_d = \frac{\omega \omega_L^{'d}}{\omega_0^{d2} - \omega^2}, \quad \alpha_d = 0. \tag{2-31b}$$

It can be seen that the characteristic impedance is a frequency-independent quantity, allowing broadband matching to 50Ω ports. Also, the phase constant exhibits a pole at the transition frequency ω_0^d between the RH band and the LH band without a gap.

The dispersion and attenuation curve and the characteristic impedance curve for the homogeneous D-CRLH TL are shown in Figure 2.10. There is a gap between the low-frequency RH band and the high-frequency LH band due to the different resonance frequencies (ω_{se}^d and ω_{sh}^d) when the D-CRLH is unbalanced. The characteristic impedance is imaginary in the stop-band and the attenuation exhibits

poles at ω_{se}^d and ω_{sh}^d. In the balanced case, since the resonance frequencies are equal to the transition frequency ($\omega_{se}^d = \omega_{sh}^d = \omega_0^d$), the gap width is reduced to zero but the phase constant β_d is discontinuous at ω_0^d. In addition, the characteristic impedance is purely real and frequency-independent, allowing broadband matching.

In the practical implementation of an artificial homogeneous LC-based D-CRLH TL, real inductors (L_R^d and L_L^d) and capacitors (C_R^d and C_L^d) in chip or printed form are required. The LC-based D-CRLH TL represents a good approximation of the homogeneous D-CRLH TL in a limited frequency band when the physical length is very small.

The stop-band cutoff frequencies can be calculated as follows:

$$\omega_{c,L/R}^d = \omega_0^d \sqrt{\frac{\left[k_d + 1 / \left(2\omega_R^d \right)^2 \right] \omega_0^{d2} \pm \sqrt{\left[k_d + 1 / \left(2\omega_R^d \right)^2 \right] \omega_0^{d4} - 4}}{2}}, \quad \text{(2-32a)}$$

$$\omega_0^d = \sqrt{\omega_{se}^d \omega_{sh}^d}, \quad \text{(2-32b)}$$

$$\omega_R^d = \frac{1}{\sqrt{L_R^d C_R^d}}, \quad \text{(2-32c)}$$

$$k_d = L_R^d C_L^d + L_L^d C_R^d, \quad \text{(2-32d)}$$

where the + sign is for the LH high-pass cutoff frequency ω_{CL}^d and the - sign is for the RH low-pass cutoff frequency ω_{CR}^d ($\omega_{CR}^d < \omega_{CL}^d$).
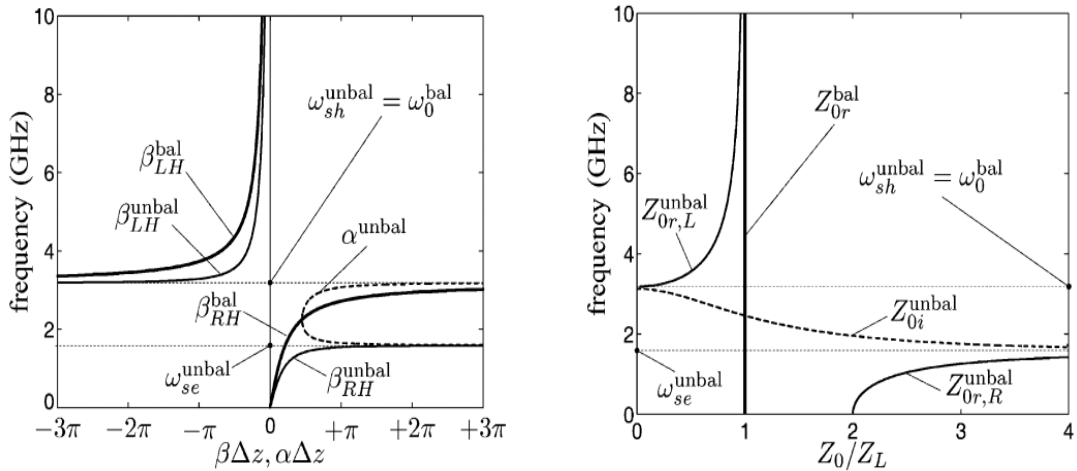
(a) Dispersion and attenuation curves.　　　(b) Characteristic impedance curve.
Figure 2.10 Characteristics of a homogeneous lossless D-CRLH TL.

In the case of a balanced LC-based D-CRLH TL, Equation (2-32a) can be simplified as follows:

$$\omega_{c,L/R}^d = \omega_0^d \sqrt{1 + \frac{\omega_L^d}{8\omega_R^d} \pm \sqrt{\frac{\omega_L^d}{4\omega_R^d}} \sqrt{1 + \frac{\omega_L^d}{16\omega_R^d}}}, \tag{2-33}$$

where

$$\omega_L^d = \frac{1}{\sqrt{L_L^d C_L^d}}, \tag{2-34a}$$

$$\lim L_R^d C_R^d \to 0 = \lim L_L^d C_L^d \to \infty = \omega_0^d. \tag{2-34b}$$

However, the gap between the RH band and the LH band always appears in a practical D-CRLH TL, since the parasitic reactance limit for closure of the gap cannot be attained in practice.

The *S*-parameter characteristic and the dispersion characteristic of the LC-based D-CRLH TL are shown in Figure 2.11. Compare with Figure 2.10, the difference is the gap between the RH band and the LH band is no longer determined by ω_{se}^d and ω_{sh}^d, but by ω_{cL}^d and ω_{cR}^d, which always follow the sequence $\omega_{cR}^d < \min(\omega_{se}^d, \omega_{sh}^d) \leq \omega_0^d \leq \max(\omega_{se}^d, \omega_{sh}^d) < \omega_{cL}^d$. Consequently, in contrast to the C-CRLH TL, a gap always presents between the RH band and the LH band in the balanced and unbalanced D-CRLH TLs. The balanced D-CRLH TL does not have gap-less infinite λ_g property as the C-CRLH TL, but it provides complementary characteristics of direct current (DC) and theoretically unlimited high-frequency propagation.

(a) Unbalanced case.

(b) Balanced case.

(c) Dispersion curve.
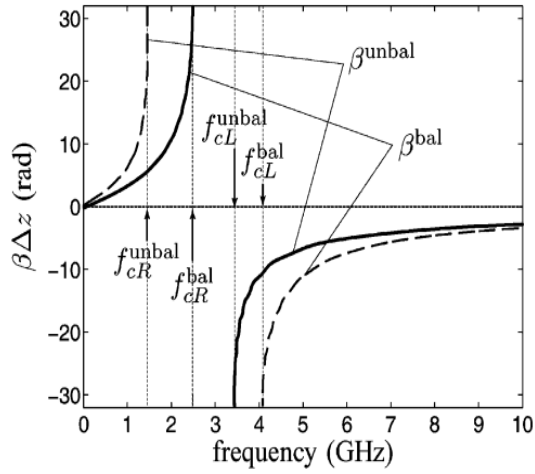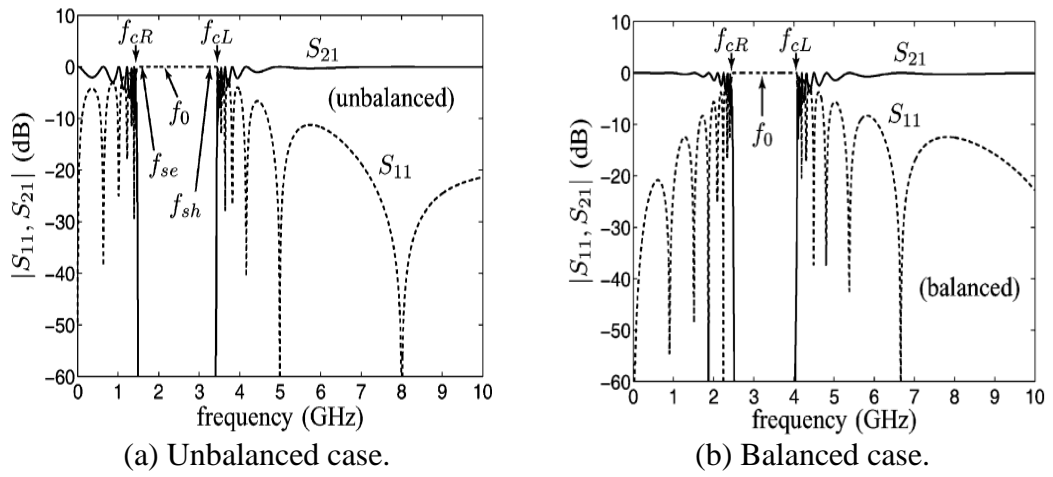
Figure 2.11 Characteristics of an LC-based D-CRLH TL.

19

2.4 Characteristics of CPW

A conventional CPW consists of a dielectric substrate and a conductor placed on the substrate, which was proposed by C. P. Wen in 1969. As shown in Figure 2.12, a signal line is placed in the middle of the dielectric substrate and two ground planes are placed on both sides of the signal line, separated by a narrow gap. In addition, the effective dielectric constant, the characteristic impedance and the attenuation are determined by the width of the signal line, the gap width and the thickness of the dielectric substrate.

The CPW is widely used in MIC and MMIC and it offers several advantages over the conventional microstrip line. For example, since the signal line and the ground planes are placed on the same plane, it is easy to connect lumped elements in series or parallel and there is no need for drilling and plating via holes to connect with the ground plane. In addition, distributed elements can be created by the parasitic effects occur on the signal lines and the dispersion effect is low in the design of microwave circuits. Therefore, the CPW has the advantages of low loss, low dispersion and easy miniaturization. However, the structural interpretation of the CPW is not simple and the abilities to adjust the low power and analysis field are not sure [10]-[12].

The characteristic impedance of the CPW has different values depending on the structure of the dielectric substrate. As shown in Figure 2.12, W is the width of the signal line and G is the gap width between the signal line and the ground planes. Moreover, T_c is the conductor thickness and H is the dielectric substrate thickness. When the CPW is lossless, the characteristic impedance Z_c and the effective dielectric constant ε_{eff} can be calculated as follows:
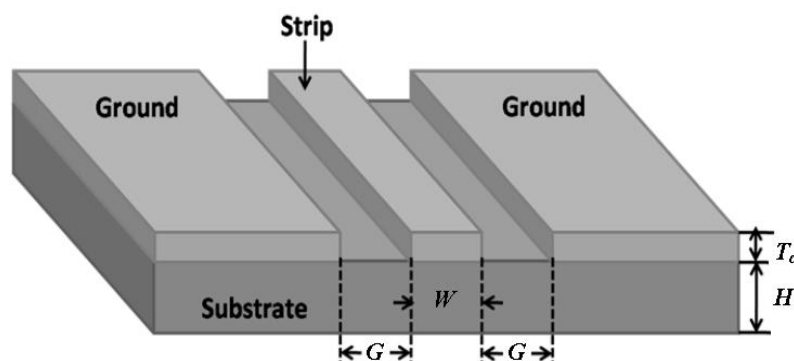
Figure 2.12 CPW geometry.

$$Z_c = \frac{30\pi}{\sqrt{\varepsilon_{eff}}} \frac{K(k_0^{'})}{K(k_0)}, \tag{2-35a}$$

$$\varepsilon_{eff} = 1 + \frac{(\varepsilon_r - 1)}{2} \frac{K(k_1)}{K(k_1^{'})} \frac{K(k_0^{'})}{K(k_0)}, \tag{2-35b}$$

where

$$k_0 = \frac{W}{W + 2G}, \tag{2-36a}$$

$$k_1 = \frac{\sinh(\pi W / 4H)}{\sinh[\pi(W + 2G)/4H]}, \tag{2-36b}$$

$$k_0^{'} = \sqrt{1 - k_0^2}, \tag{2-36c}$$

$$k_1^{'} = \sqrt{1 - k_1^2}, \tag{2-36d}$$

$K(\ )$ is the complete elliptic integral of the first kind and ε_r is the relative permittivity.

According to [13], if the substrate thickness H is less than twice the gap width G, 10-15% deviation occurs when the dielectric substrate is infinite. And the attenuation and crosstalk caused by leakage power can be avoided by using a thin dielectric substrate. Therefore, the propagation characteristics of lines with high characteristic impedance and large gap width on thin substrates should be determined using Equation (2-35) above.

2.4.1 CPW Open Circuit

As shown in Figure 2.13(a), a CPW open circuit is formed by ending the center signal line a short distance before the slot ends. An electric field presents at the gap between the terminated signal line and the surrounding ground plane, so that capacitive reactance is generated. Figure 2.13(b) shows the equivalent circuit for the CPW open circuit.

When $S \leq 0.1(W + 2G)$, the open circuit capacitance C_{oc} of the equivalent circuit can be calculated as follows:

$$C_{oc} = C_{oc}^{air} \varepsilon_{eff}, \tag{2-37}$$

where

$$C_{oc}^{air} = \frac{2\varepsilon_0}{\pi}\left\{(W+G)\left[\frac{\ln(\eta+\sqrt{1+\eta^2})}{\eta}+\ln\left(\frac{1+\sqrt{1+\eta^2}}{\eta}\right)\right.\right.$$
$$\left.\left.-\frac{1}{3}\left(\frac{1}{1+\sqrt{1+\eta^2}}+\frac{1}{\eta+\sqrt{1+\eta^2}}\right)\right]-\left(W+\frac{2}{3}G\right)\right\},$$

$$\text{(2-38a)}$$

$$\eta = \frac{S}{W+G}. \qquad\qquad \text{(2-38b)}$$

2.4.2 CPW Short Circuit

As shown in Figure 2.14(a), as the current flows around the termination of the signal line in a CPW short circuit, the magnetic energy stored behind the termination and inductive reactance is produced. And Figure 2.14(b) shows the equivalent circuit for the CPW short circuit. The short circuit inductance L_{sc} of the equivalent circuit can be calculated as follows:

$$\text{L}_{sc} = \left(\frac{2}{\pi}\right)\varepsilon_0\varepsilon_{eff}\left(a+b\right)Z_0^2\left[1-\frac{1}{\cosh\left(\frac{60\pi^2}{Z_0\sqrt{\varepsilon_{eff}}}\right)}\right], \qquad \text{(2-39)}$$

where $2a=W$ and $2b=W+2G$.

2.4.3 Step Change in the Width of Center Strip Conductor of CPW

As shown in Figure 2.15(a), the discontinuity due to the step change in the signal line width perturbs the normal CPW electric and magnetic fields and gives rise to additional reactances. And by using the hybrid finite element method, this step change structure can be modeled as a T-network, which consists of two series inductances and a shunt capacitance.

Assuming that the conductor thickness T_c is constant, the values of the inductance and the capacitance get larger when the ratio W_2/d is larger the ratio W_1/d. When the ratio W_2/d is constant, the inductance value decreases as T_c increases, but the capacitance value increases at the same time. In addition, the reduction rate of the inductance is greater than the growth rate of the capacitance [11]-[12].

(a) Physical geometry.　　　　　　(b) Equivalent circuit.
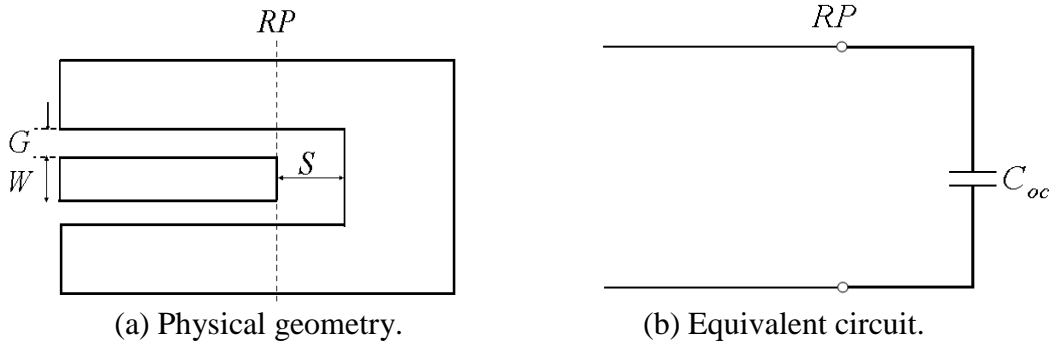
Figure 2.13 CPW open circuit.

(a) Physical geometry.　　　　　　(b) Equivalent circuit.
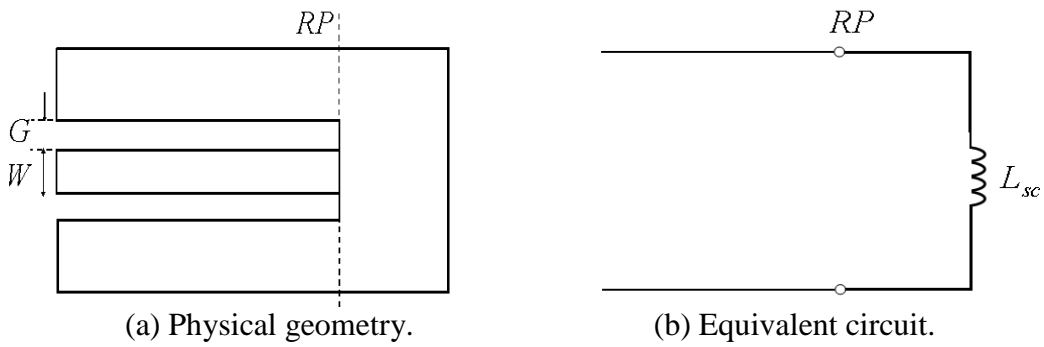
Figure 2.14 CPW short circuit.

(a) Physical geometry.　　　　　　(b) Equivalent circuit.
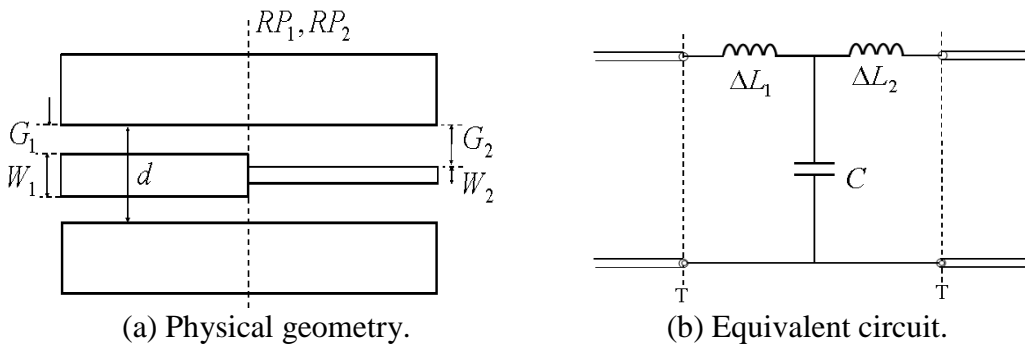
Figure 2.15 Step-changed geometry in the width of center strip conductor of a CPW.

(a) Calculated equivalent inductance.　　(b) Calculated equivalent capacitance.
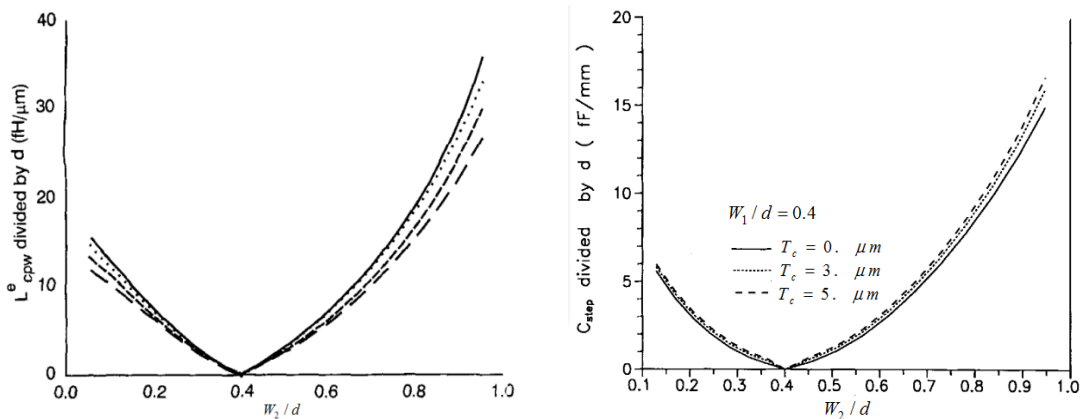
Figure 2.16 Calculated equivalent inductance and capacitance of symmetric step change as a function of a normalized width W_2/d [16]-[17].

2.4.4 CBCPW

A CBCPW is a variant of the CPW that an extra ground plane is implemented on the bottom layer. As shown in Figure 2.17, the CBCPW consists of a dielectric substrate and two conductors placed on both sides of the substrate. The conductor on the top layer formed a center signal line separated by a narrow gap from two ground planes on either side and the conductor on the bottom layer formed a ground plane. The characteristic impedance of the CBCPW can be calculated as follows [14]:

$$Z_c = \frac{60\pi}{\sqrt{\varepsilon_{eff}}} \frac{1}{\dfrac{K(k_0)}{K(k_0')} + \dfrac{K(k_1)}{K(k_1')}}, \tag{2-40a}$$

$$\varepsilon_{eff} = \frac{1 + \varepsilon_r \dfrac{K(k_0')}{K(k_0)} \dfrac{K(k_1)}{K(k_1')}}{1 + \dfrac{K(k_0')}{K(k_0)} \dfrac{K(k_1)}{K(k_1')}}, \tag{2-40b}$$

where $a = \dfrac{W}{2}, b = \dfrac{W}{2} + G$ and

$$k_0 = \frac{a}{b}, \tag{2-41a}$$

$$k_1 = \tanh\left(\frac{\pi a}{2H}\right)\tanh\left(\frac{\pi b}{2H}\right). \tag{2-41b}$$
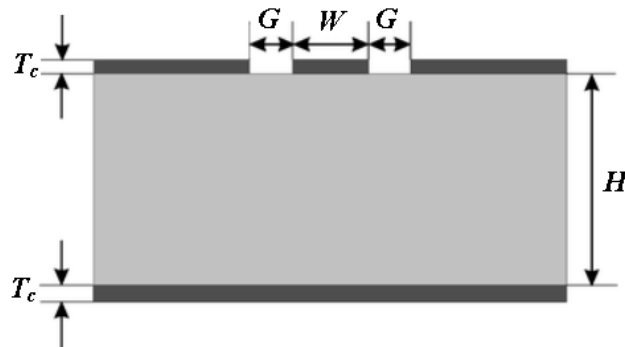
Figure 2.17 CBCPW geometry.

Chapter 3   Unit Cell Design Based on C-CRLH MTM TL

3.1 Unit Cell with High-Pass Property Based on C-CRLH FCPW

3.1.1 LH Unit Cell Based on FCPW and Simulation Results

A LH unit cell is designed on folded coplanar waveguide (FCPW) with C-CRLH structure and the physical geometry is shown in Figure 3.1 [18]-[19]. On the top and bottom layers of the FCPW, both of which are structured as CPW. The CPW structure on the top layer is transformed by connecting a metal rectangular grounded patch (RGP) with a side ground plane, as shown in Figure 3.1(a). As shown in Figure 3.1(b), metal rectangular conductor patches (RCPs) are installed on the bottom layer of the FCPW and they connect with feeder lines by via holes.

The LH unit cell is fabricated on a printed circuit board (PCB) with the relative dielectric constant ε_r of 2.5, the dielectric substrate thickness H of 0.787mm and the conductor thickness T_c of 35um. Since only the top layer connects the input and output ports directly, the values of the signal feeder line width W and the gap width G between the feeder line and the side ground planes can be calculated by the tool Linecalc in the advanced design system (ADS), responding to 50Ω characteristic impedance of a CPW structure. The calculated results are W = 8.74mm and G = 0.3mm.

As shown in Figure 3.1, the LH unit cell is centrally symmetric based on the central axis of the unit cell. When the signal transmits along the LH unit cell, the series component C_L is generated in proportion to the relative area of the RGP and RCP, and the parallel component L_L is created at the narrow line which connects the RGP to the side ground plane. According as the signal transmits along the same geometry repeatedly, those components are generated again. Therefore, the RH characteristic is suppressed, and the LH characteristic dominates on the LH unit cell. By tuning the values of the parameters L_1, L_2, D, D_1, S_1 and S_2, the cutoff frequency and the characteristics of pass-band and stop-band can be adjusted.

The equivalent circuits for the LH unit cell are shown in Figure 3.2. And the equivalent values of the capacitances ($C_L = (C_s // C_{cp2}) // (C_{cp1}/2)$ and $C_R = C_p // C_{cp3}$) and the inductance ($L_L = L_p$) can be calculated according to [21] as

$$C_s = \varepsilon_0(\varepsilon_{eff}+1)\frac{(L_2-D_1)(W-2S_2)}{H}, \qquad (3\text{-}1a)$$

$$C_p = C_{oe} \times 2L_2, \qquad (3\text{-}1b)$$

$$C_{cp1} = \varepsilon_0(\varepsilon_{eff2}+1)\frac{T_c(W-2S_1)}{2D_1}, \qquad (3\text{-}1c)$$

$$C_{cp2} = \varepsilon_0(\varepsilon_{eff1}+1)\frac{T_c(W-2S_2)}{D}, \qquad (3\text{-}1d)$$

$$C_{cp3} = \varepsilon_0(\varepsilon_{eff1}+1)\frac{2T_c(L_2-K)}{S_2+G}, \qquad (3\text{-}1e)$$

$$L_p = C_p'^2 Z_c = (C_{oe}' \times 2K)^2 Z_c, \qquad (3\text{-}1f)$$
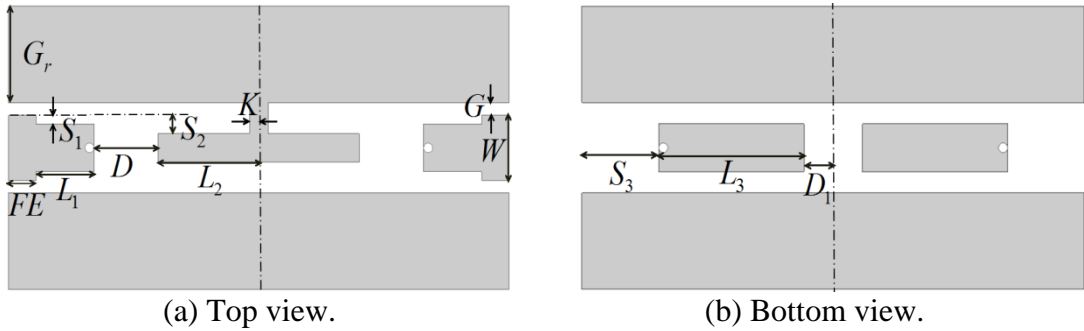
(a) Top view.   (b) Bottom view.
Figure 3.1 Physical geometries of LH unit cell.
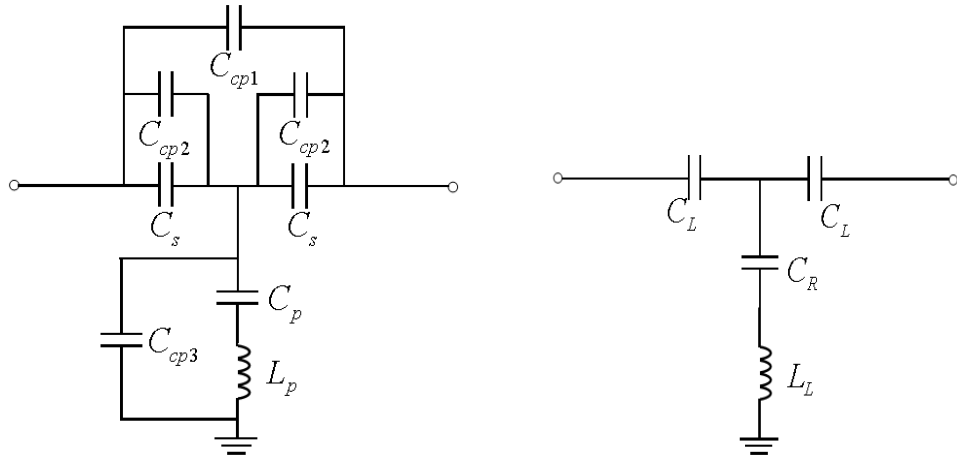
(a) Detailed equivalent circuit.   (b) Approximate equivalent circuit.
Figure 3.2 Equivalent circuits for LH unit cell.

where C_s is created between the overlapped parallel patches (RGP and RCPs), C_p is distributed on the RGP and L_p is created on the narrow line which connects the RGP to the side ground plane. C_{cp3} is created at the interval S_2+G between the RGP and the side ground plane. And C_{cp1} and C_{cp2} are created at the interval D_1 between two RCPs and the interval D between the feeder line and the RGP, respectively. However, the values of C_{cp1}, C_{cp2}, C_{cp3} can be ignored since they have little effect on the characteristics of the equivalent circuit. On the other hand, ε_0 is the permittivity of free space and the values of the effective permittivity ε_{eff} and the characteristic impedance Z_c can be calculated responding to the sizes of the signal line width and the gap width between the signal line and the side ground planes, according to [22]. C_{oe} and C_{oe}' are the inherent capacitances of the FCPW, which can be also calculated by the equations in [22]. However, the equations in [22] do not exactly match the LH unit cell because the proposed structure in [22] is not totally the same with it. Therefore, the values of the inherent capacitances are not correct and Equation (3-1f) should be modified by the approximation process, based on the simulation results.

The influences of the parameters L_1, L_2, D_1 and S_2 are investigated and Figure 3.3 shows the simulated return loss characteristics done by high frequency structural simulator (HFSS). As the value of L_1 increases doubled and quadrupled, the resonant frequencies do not change much. That is, L_1 does not have much effect on the characteristics change. However, as the value of L_2 increases, the resonant frequencies change much. When L_2 changes to 12.7mm ($\lambda_g/8$), two resonant frequencies get closer and a pass-band becomes visible. In addition, as the values of D_1 and S_2 increase, the resonant frequencies decrease slowly due to the series capacitance increases. Moreover, when the length of D_1 gets shorter, the magnitude of S-parameter S_{11} in the pass-band gets better.

The S-parameter characteristics of the LH unit cell and the equivalent circuit are simulated by HFSS and ADS, respectively. The S-parameter simulation results are plotted in Figure 3.4. And Table 3.1 shows the electrical and physical lengths of the parameters in the LH unit cell. As shown in Figure 3.4, the LH unit cell exhibits high-pass property. By changing the lengths of the parameters, the cutoff frequency

and the *S*-parameter characteristics can be changed to get the desired high-pass property. Comparing the simulation results of the LH unit cell with the ones of the equivalent circuit, the *S*-parameter graphs show good agreements. Table 3.2 gives the cutoff frequencies of the LH unit cell and the equivalent circuit, and the error rates, which are calculated based on the cutoff frequencies. Among the data, Case I gets the best error rate and other three are similar.

(a) L_1.   (b) L_2.

(c) D_1.   (d) S_2.
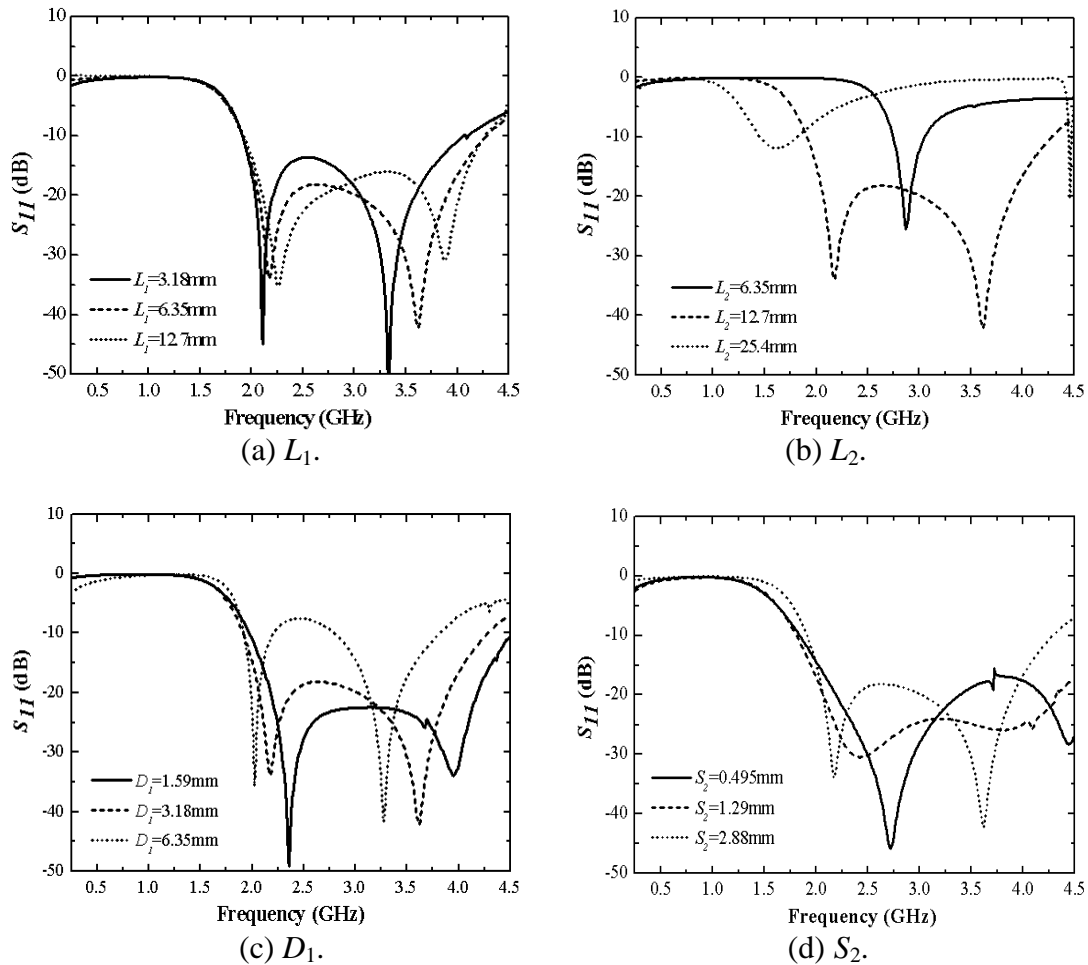
Figure 3.3 Return loss characteristics as a function of geometrical parameters.

Table 3.1 Electrical and physical lengths according to cases of LH unit cell.

	Electrical length (f_0=1.87GHz)			Physical length (unit: mm)		
	L_2	S_2+G	D_1	L_2	S_2 (G=0.3)	D_1
Case I	$\lambda_g/8$	$\lambda_g/64$	$\lambda_g/32$	12.7	1.29	3.18
Case II	$\lambda_g/16$	$\lambda_g/64$	$\lambda_g/32$	6.35	1.29	3.18
Case III	$\lambda_g/8$	$\lambda_g/64$	$\lambda_g/16$	12.7	1.29	6.35
Case IV	$\lambda_g/8$	$\lambda_g/32$	$\lambda_g/32$	12.7	2.88	3.18

(a) Case I.   (b) Case II.

(c) Case III.   (d) Case IV.
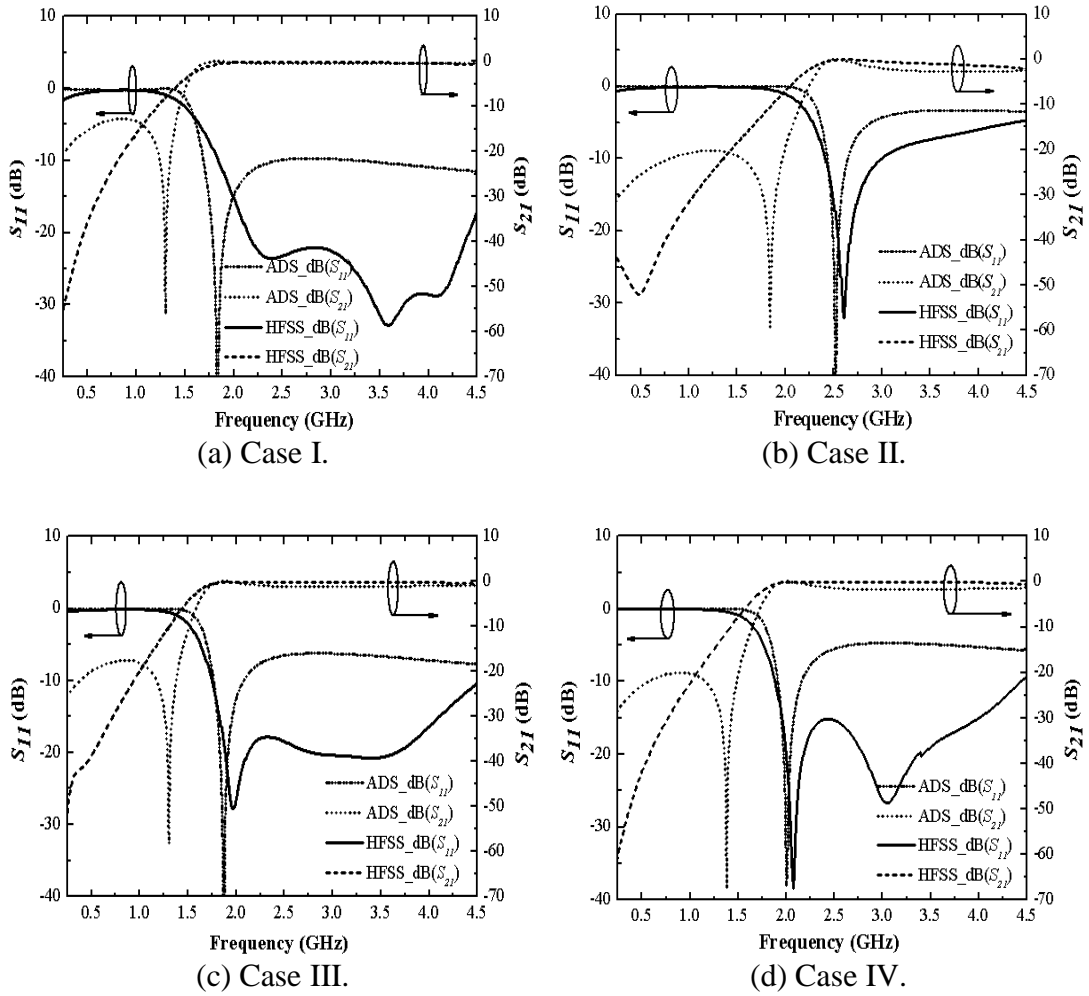
Figure 3.4 *S*-parameter simulation results of LH unit cell according to cases.

Table 3.2 Error rates of *S*-parameter simulation results according to cases.

	Cutoff freq. of LH unit cell	Cutoff freq. of equivalent circuit	Error rate
Case I	1.55GHz	1.57GHz	1.29%
Case II	2.20GHz	2.32GHz	5.45%
Case III	1.56GHz	1.65GHz	5.77%
Case IV	1.70GHz	1.80GHz	5.88%

Comparing the *S*-parameter simulation results done by HFSS in Figure 3.4, Case I shows the best characteristics that return loss in the pass-band is more than 17.01dB. At the same time, the magnitude of S_{21} curve is maximum flatness in the pass-band and less than -54.88dB in the stop-band. When the cutoff frequency is 1.55GHz, the length of L_2 in Case I is $\lambda_g/8$, S_2 is $\lambda_g/64$ and D_1 is $\lambda_g/32$. In general, the lengths of filter stubs are being $\lambda_g/8$ [24] or $\lambda_g/4$ [25]. Therefore, the LH unit cell is more advantageous to achieve miniaturization in filter design.

3.1.2 DLH Unit Cell Based on FCPW and Simulation Results

As shown in Figure 3.5, the geometrical configurations are called dual left-handed (DLH) unit cell structure, which is opposite to the structure of the LH unit cell [19]. In the DLH unit cell, the metal RCPs are placed on the top layer of the FCPW. And the RGP, which connects with a side ground plane, is placed on the bottom. Because the series component C_L can be generated without via holes in the DLH unit cell, the DLH unit cell is easier to be manufactured on the PCB than the LH unit cell.

The equivalent circuit for the DLH unit cell is same with Figure 3.2(b). And the equivalent values of the capacitances (C_L and C_R) and the inductance (L_L) can be calculated as

$$C_L = \varepsilon_0 (1 + \varepsilon_{eff}) \frac{(W - 2S)L}{H} + C_{oe}L, \qquad (3\text{-}2a)$$

$$C_R = C_{oe}(2L + D), \qquad (3\text{-}2b)$$

$$L_L = C_p^{'2} Z_c = (C_{oe}^{'} \times 2K)^2 Z_c, \qquad (3\text{-}2c)$$

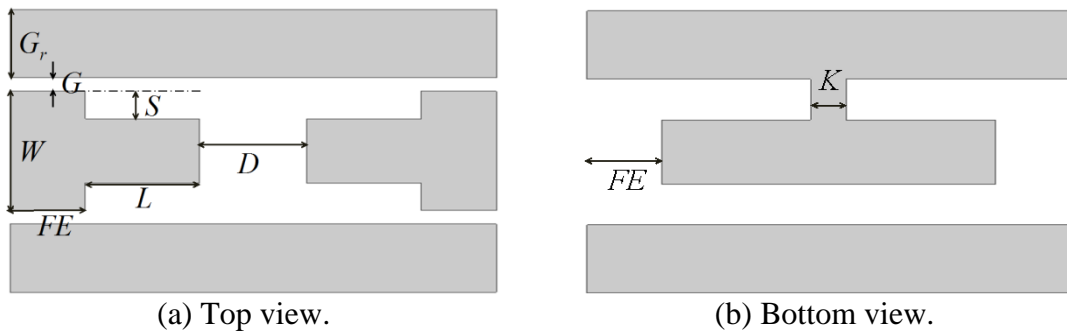(a) Top view.   (b) Bottom view.
Figure 3.5 Physical geometry of DLH unit cell.

where C_L is created between the overlapped parallel patches (RGP and RCPs), C_R is distributed on the RGP and L_L is created at the narrow line which connects RGP to the side ground plane. Additionally, the inherent capacitances C_{oe} and $C_{oe}^{'}$, the characteristic impedance Z_c and the effective permittivity ε_{eff} can be calculated by the equations in [22]. Since the calculated inherent capacitances have an error with the real values, Equation (3-2c) should be modified by the approximation process based on the simulation results.

The influences of the parameters L, D and S are investigated and Figure 3.6 shows the simulated return loss characteristics. As L gets close to 6.4mm ($\lambda_g/16$), the two resonant frequencies get closer and a pass-band appears. And as D increases doubled and quadrupled, the resonant frequencies decrease due to the shunt capacitance increases. Additionally, when the length of S is shorter than 1.3mm ($\lambda_g/64$), the resonant frequencies decrease slowly. And when S is longer than 1.3mm ($\lambda_g/64$) the resonant frequencies change a little, but the magnitude of the pass-band gets worse.

The S-parameter simulation results are plotted in Figure 3.7 and the electrical and physical lengths of the parameters in the DLH unit cell are shown in Table 3.3. Comparing the S-parameter simulation results of the DLH unit cell with the ones of the equivalent circuit, the graphs have similar characteristics. Table 3.4 gives the cutoff frequencies of the DLH unit cell and the equivalent circuit, and the error rates are calculated based on the cutoff frequencies. Among the data, Case VI gets the smallest error rate and Case VIII has the worst result. Comparing the parameter lengths in Table 3.3, only the value of S in Case VI is different from Case VIII. Since the inherent capacitances are calculated based on the signal line width, S has the main effect on the value of the inherent capacitances. Thus, the energy accumulated on the RGP is less than the calculated value.

Comparing the four simulation results of the DLH unit cell done by HFSS in Figure 3.7, Case VIII exhibits the best characteristics that the return loss in the pass-band is more than 18.2dB until 4GHz, and the magnitude of S_{21} curve is maximum flatness. When the cutoff frequency is 1.65GHz, the length of L in Case V is $\lambda_g/16$, S

is shorter than $\lambda_g/128$ and D is $\lambda_g/8$. That is, the DLH unit cell is advantageous to achieve miniaturization in filter design.

(a) L.

(b) D.

(c) S.
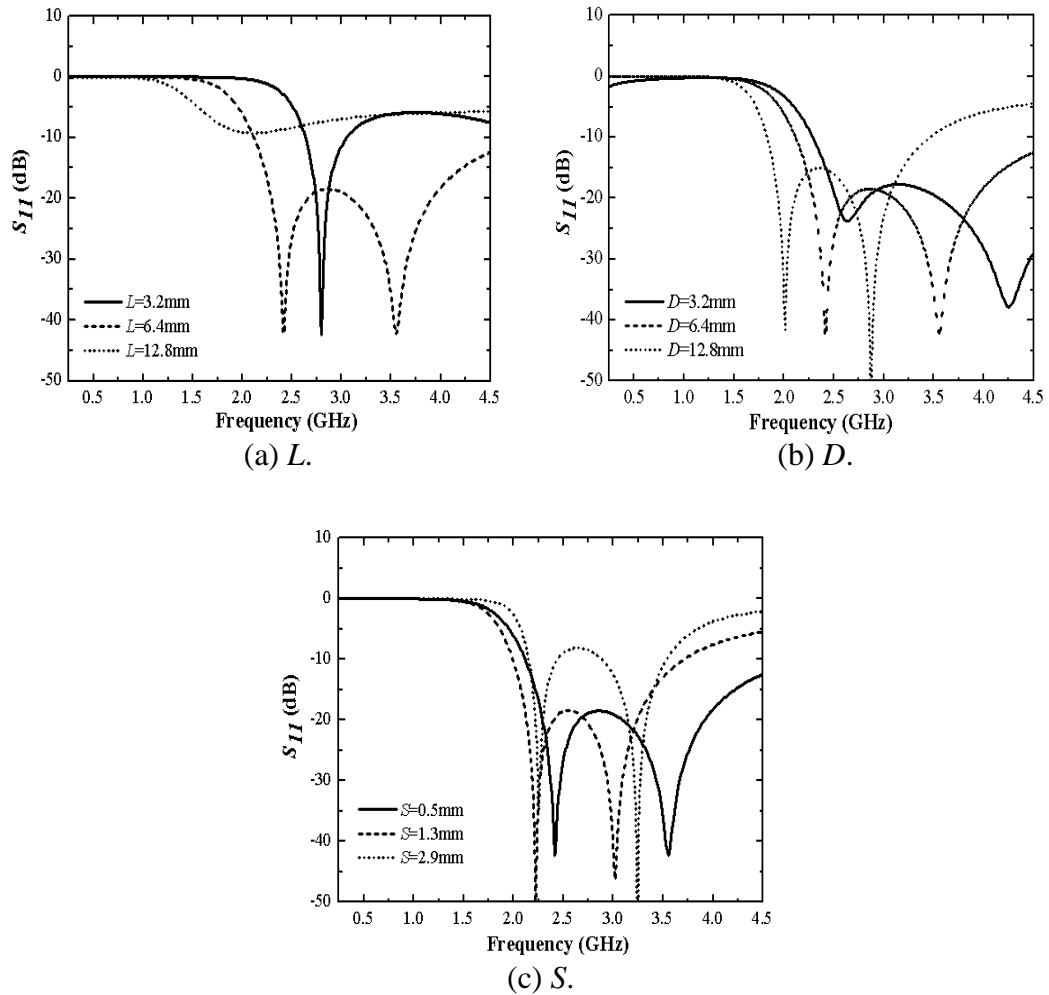
Figure 3.6 Return loss characteristics as a function of geometrical parameters.

Table 3.3 Electrical and physical lengths according to cases of DLH unit cell.

	Electrical length (f$_0$=1.85GHz)			Physical length (unit: mm)		
	L	$S+G$	D	L	S (G=0.3mm)	D
Case V	$\lambda_g/16$	$\lambda_g/128$	$\lambda_g/8$	6.4	0.5	12.8
Case VI	$\lambda_g/16$	$\lambda_g/64$	$\lambda_g/16$	6.4	1.3	6.4
Case VII	$\lambda_g/8$	$\lambda_g/128$	$\lambda_g/16$	12.8	0.5	6.4
Case VIII	$\lambda_g/16$	$\lambda_g/128$	$\lambda_g/16$	6.4	0.5	6.4

(a) Case V.

(b) Case VI.

(c) Case VII.

(d) Case VIII.
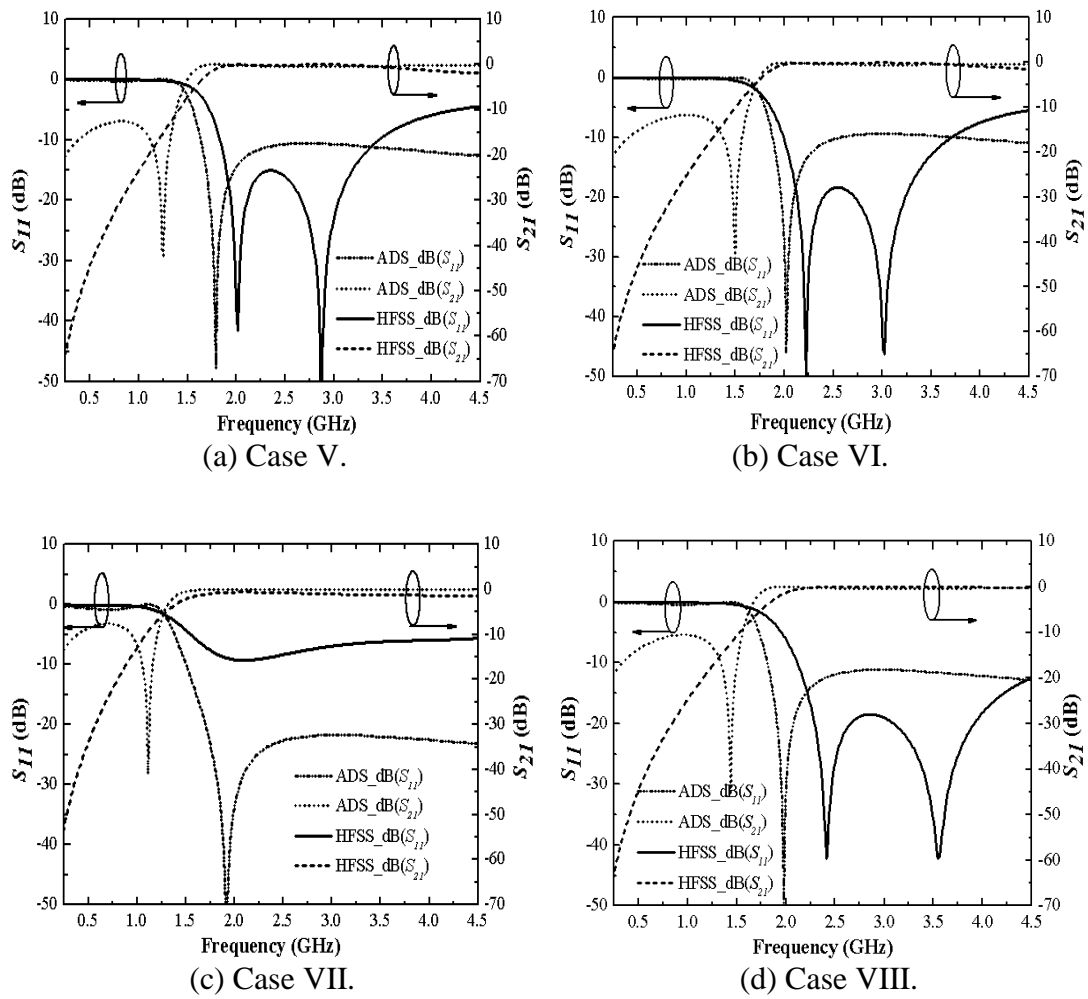
Figure 3.7 *S*-parameter simulation results of DLH unit cell according to cases.

Table 3.4 Error rates of *S*-parameter simulation results according to cases.

	Cutoff freq. of DLH unit cell	Cutoff freq. of the equivalent circuit	Error rate
Case V	1.65GHz	1.51GHz	8.48%
Case VI	1.78GHz	1.76GHz	1.12%
Case VII	1.41GHz	1.33GHz	5.67%
Case VIII	1.86GHz	1.68GHz	9.68%

33

When the cutoff frequencies of the LH unit cell and the DLH unit cell are the same, the *S*-parameter simulation results are compared, shown in Figure 3.8. In the stop-band, the S_{21} curves increase straightly and the skirt effects are similar. In the pass-band, the return loss of the DLH unit cell is more than 13dB in the pass-band of 2.2 ~ 4.5GHz, and of the LH unit cell is more than 10dB in the range of 2.05 ~ 4.5GHz. In addition, the physical dimensions of the LH unit cell and the DLH unit cell are shown in Table 3.5 and Table 3.6. The total length of the DLH unit cell is 27.04mm and the LH unit cell is 54.70mm, which is twice as large as the DLH unit cell. In summary, the DLH unit cell gets better characteristics than the LH unit cell.
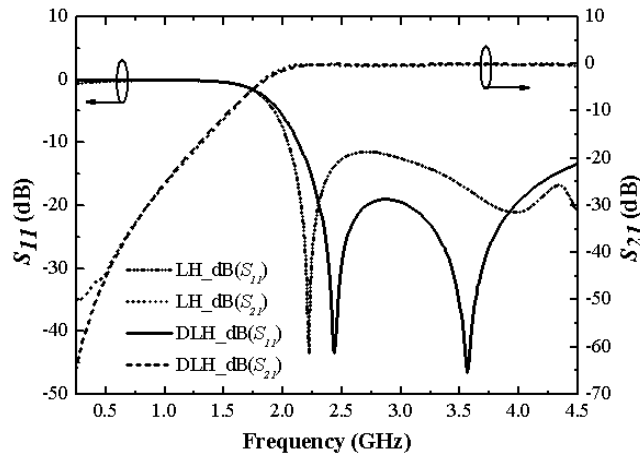
Figure 3.8 *S*-parameter simulation results of LH unit cell and DLH unit cell.

Table 3.5 Physical dimensions of LH unit cell. (unit: mm)

Parameters	L_1	L_2	L_3	Gr	FE	S_1	S_2	S_3	K
Values	6.35	11	17.52	10	3	0.5	2.88	8.35	1
Parameters	D	D_1	W	G	T_c	H			
Values	7	3.18	8.74	0.3	35	0.787			

Table 3.6 Physical dimensions of DLH unit cell. (unit: mm)

Parameters	L	K	D	G_r	FE	S	G	W
Values	6.35	2	6	5	4.2	0.5	0.3	8.74

In order to identify if the C-CRLH effect occurs in the LH unit cell and the DLH unit cell, the dispersion diagram is simulated by HFSS with the phase constant calculated by the S parameters as follows:

$$\beta_p = \cos^{-1}(\frac{1 - S_{11}S_{22} + S_{12}S_{21}}{2S_{21}}). \tag{3-3}$$

Figure 3.9 shows the direction of the propagation in the LH unit cell and the DLH unit cell. As shown in Figure 3.9, the proposed unit cells exhibit the C-CRLH characteristics and Table 3.7 gives the bands where the LH or RH effect occurs.

(a) LH unit cell. (b) DLH unit cell.
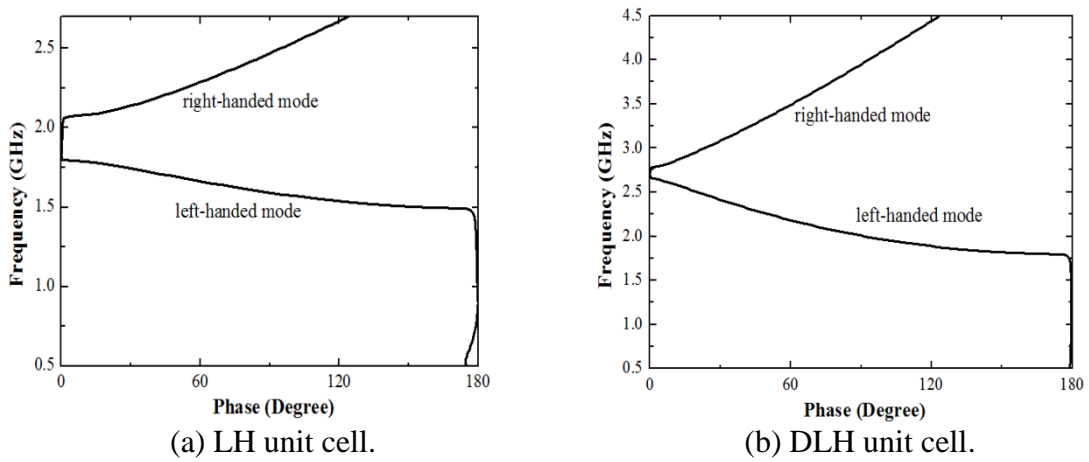Figure 3.9 Dispersion characteristics of LH unit cell and DLH unit cell.

Table 3.7 Bandwidth of LH range and RH range.

|	LH bandwidth	RH bandwidth
LH unit cell	1.46 ~ 1.81GHz	2.05 ~ 3.05GHz
DLH unit cell	1.76 ~ 2.66GHz	2.77 ~ 4.5GHz

In the LH unit cell and DLH unit cell, the energy distributions of the electric field correspond to the accumulated energy distribution of the series composition C_L that generated according to the relative area of the RGP and the RCPs, as shown in Figure 3.10(a) and Figure 3.11(a). As time elapses, the electric energy turns to be the magnetic energy. The magnetic energy distribution corresponds to the accumulated energy distribution of the shunt circuit component L_L, which is created by the narrow line which connects the RGP to the side ground plane, as shown in Figure 3.10(b) and Figure 3.11(b). This process is done repeatedly over time, while the signal energy is transmitted from the input port to the output port. Therefore, the energy transference and suppression of the input signal are achieved by the inductances and capacitances, which form the LH characteristics. And according to the values of the inductances and capacitances, the unit cells show the nature of an HPF. Eventually, the LH unit cell and the DLH unit cell get the characteristics of preserving the input electromagnetic energy and transmitting the energy to the output port without loss, as well as the characteristic of high-pass frequency selectivity.
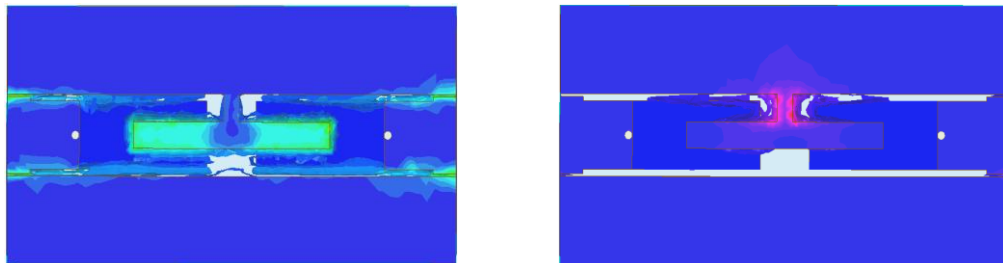
(a) Energy distribution of electric field.   (b) Energy distribution of magnetic field.
Figure 3.10 Energy distributions of LH unit cell.
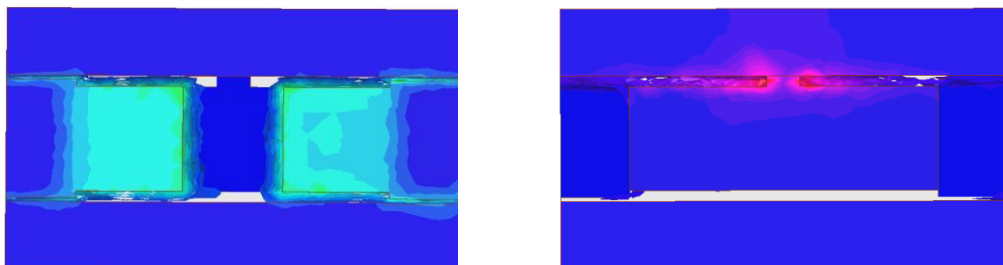
(a) Energy distribution of electric field.   (b) Energy distribution of magnetic field.
Figure 3.11 Energy distributions of DLH unit cell.

3.1.3 Measurement Results of LH Unit Cell and DLH Unit Cell

The layout patterns of the LH unit cell and the DLH unit cell are shown in Figure 3.12 and Figure 3.13, respectively. The unit cells are fabricated on the substrates made by Taconic, through the photosensitizing, etching, plating and assembling processes. After these production processes, the characteristics of the LH unit cell and the DLH unit cell are measured by vector network analyzer of N5230A.

The comparisons of *S*-parameter simulation and measurement results of the LH unit cell and the DLH unit cell are shown in Figure 3.14. The graphs have similar shapes, but the cutoff frequencies are partially mismatched. The measured result shifted to the high frequencies because of the imperfection of the ground effect, which reduces the electrical energy accumulated between the RGP and RCPs. The measured S_{11} magnitude of the LH unit cell is below -9.88dB in the range beyond 2.05GHz, but tends to rise slightly beyond 4.05GHz. And the measured S_{11} magnitude of the DLH unit cell is below -10dB in the range of 2.52 ~ 2.9GHz and the range beyond 4.23GHz, but above -8dB from 3.04GHz to 4.07GHz, which is not good enough as a filter. In the pass-band, the insertion loss of the LH unit cell is less than 0.74dB and of the DLH unit cell is less than 1.76dB.
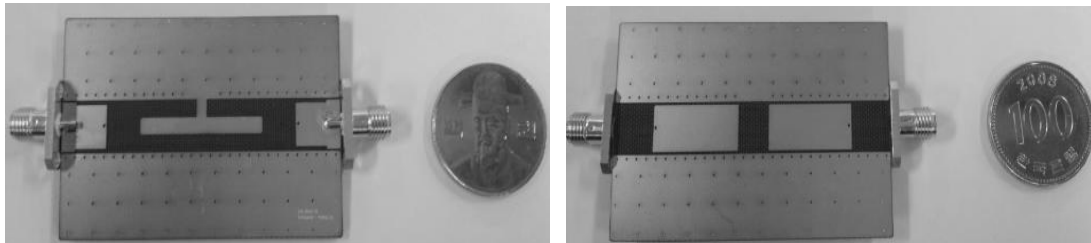
(a) Top view.   (b) Bottom view.
Figure 3.12 Fabricated LH unit cell.
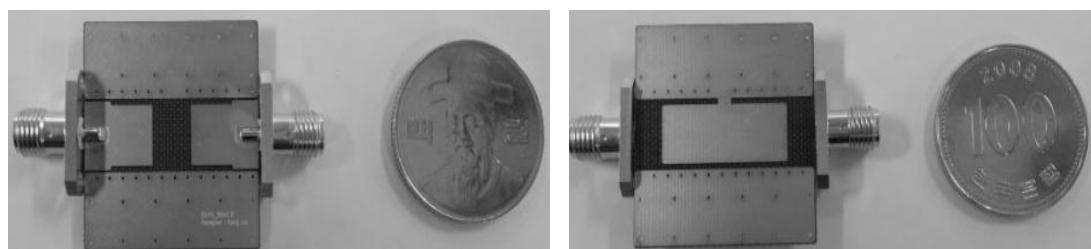
(a) Top view.   (b) Bottom view.
Figure 3.13 Fabricated DLH unit cell.

Comparing the measurement results of the LH unit cell and the DLH unit cell shown in Figure 3.15, the magnitudes of S_{21} curves in the stop-band increase rapidly and have similar shapes. However, the LH unit cell exhibits deeper rejection than the DLH unit cell in the pass-band. Even so, the DLH unit cell is better for HPF design because the ripples of S_{11} curve in the pass-band get a regulation and it is favorable to get a broad pass-band. As long as the ground plane can be made good enough, the return loss will be on the increase and the DLH unit cell can be used for compact HPF design.
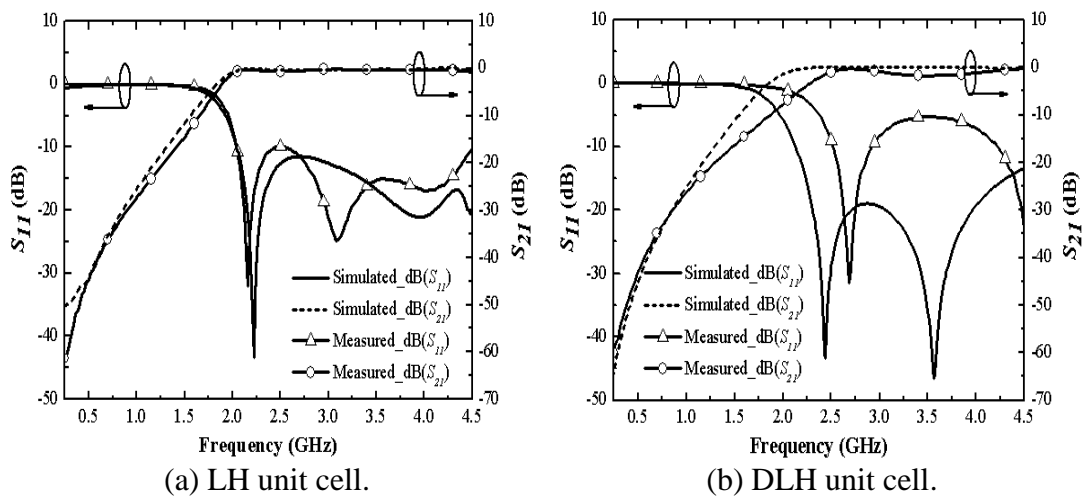

(a) LH unit cell.   (b) DLH unit cell.

Figure 3.14 *S*-parameter simulation and measurement results of LH unit cell and DLH unit cell.
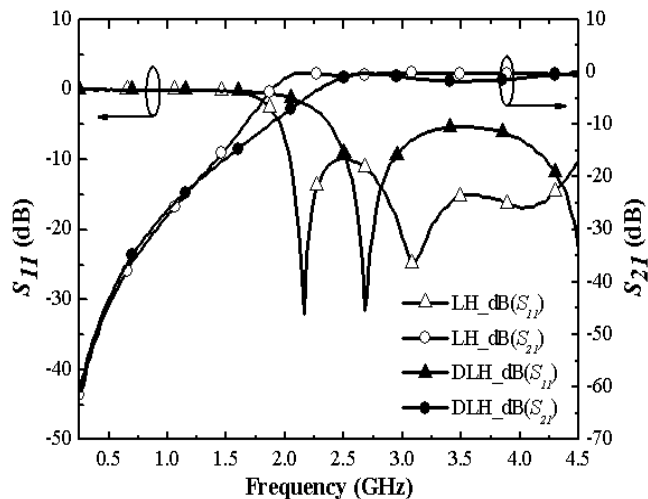

Figure 3.15 Measurement results of LH unit cell and DLH unit cell.

38

3.2 Unit Cell with Low-Pass Property Based on C-CRLH CBCPW

3.2.1 RH Unit Cell Based on CBCPW

A RH unit cell based on C-CRLH CBCPW is proposed and its physical geometry is shown in Figure 3.16 [18], [20]. The geometry consists of a dielectric substrate between two metallic layers. And the top layer is composed of two ground planes and a signal line, while the bottom layer is a ground plane only. This structure is designed on a PCB with the relative dielectric constant ε_r of 2.5 and the dielectric substrate thickness H of 0.787mm. And the width of the feeder line W is 8.74mm, and the gap width between the feeder line and the round planes on the same layer G is 0.3mm, which are calculated by the tool Linecalc in ADS.

As shown in Figure 3.16, the input port is symmetric with the output port, based on the central axis of the unit cell. When the signal transmits through the broad signal line, the parallel component C_R is generated between the signal line and the ground plane on the bottom layer. Then the signal transmits through the narrow signal line, the series component L_R is distributed on it. According as the signal transmits along the same geometry repeatedly, those components are generated again. Between the broad signal lines, coupling capacitance C_L can be generated when the value of the parameter D is very small. And L_L can be achieved along the stub lines toward the side ground planes. By tuning the sizes of L_1, L_2, L_3, D, K, S_1, S_2 and T, the cutoff frequency and the S-parameter characteristics can be changed. In other words, the values of the components L_R, C_R (C_{R1} and C_{R2}), L_L, which are shown in Figure 3.17(b), change with the sizes of the unit cell. As a result, the RH characteristic dominates on the RH unit cell, and the LH characteristic is suppressed. As shown in Figure 3.17, the equivalent circuit values of the inductances ($L_R = L_s$ and $L_L = L_p$) and the capacitances ($C_{R1} = C_{p1} + C_{p2}$ and $C_{R2} = 2C_{p2} + C_{p3}$) can be calculated according to [21] as

$$L_s = \frac{Z_C \sin(2\pi D / \lambda_g)}{\omega_0} \approx \left. \frac{Z_c 2\pi D}{\lambda_g \omega_0} \right|_{D < \frac{\lambda_g}{8}} = \frac{Z_c D \sqrt{\varepsilon_{eff}}}{c}, \qquad (3\text{-}4a)$$

$$C_p = \frac{\tan(2\pi L_3 / \lambda_g)}{Z_c \omega_0} \approx \left. \frac{\pi L_3}{Z_c \lambda_g \omega_0} \right|_{L_3 < \frac{\lambda_g}{8}} = \frac{L_3 \sqrt{\varepsilon_{eff}}}{Z_c c}, \qquad (3\text{-}4b)$$

$$L_p = C_p Z_c^2 / 2 \qquad (3\text{-}4c)$$

$$C_{p2} = \frac{\tan(\pi D / \lambda_g)}{Z_c \omega_0} \approx \left. \frac{\pi D}{Z_c \lambda_g \omega_0} \right|_{D < \frac{\lambda_g}{8}} = \frac{D \sqrt{\varepsilon_{eff}}}{2 c Z_c}, \qquad (3\text{-}4d)$$

$$C_{p1} = \varepsilon_0 (\varepsilon_{eff} + 1) \frac{L_1 (W - S_1)}{H}, \qquad (3\text{-}4e)$$

$$C_{p3} = \varepsilon_0 (\varepsilon_{eff} + 1) \frac{2 L_2 (W + S_2)}{H}, \qquad (3\text{-}4f)$$
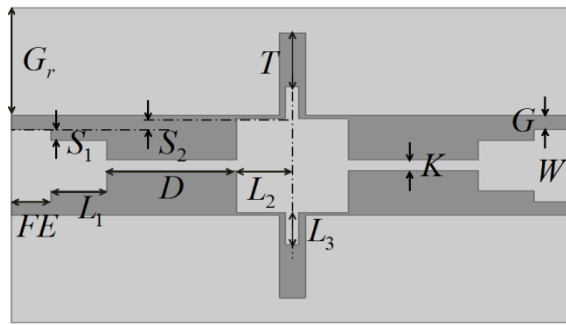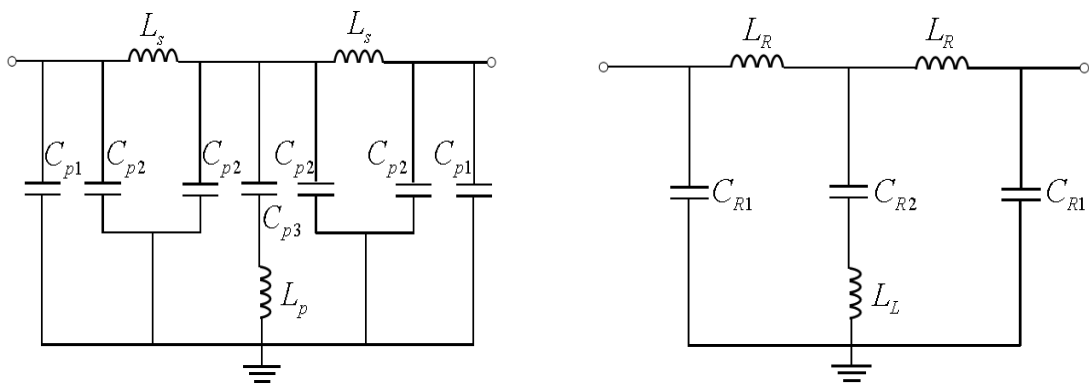

Figure 3.16 Physical geometry of RH unit cell.

(a) Detailed equivalent circuit.　　　　(b) Approximate equivalent circuit.

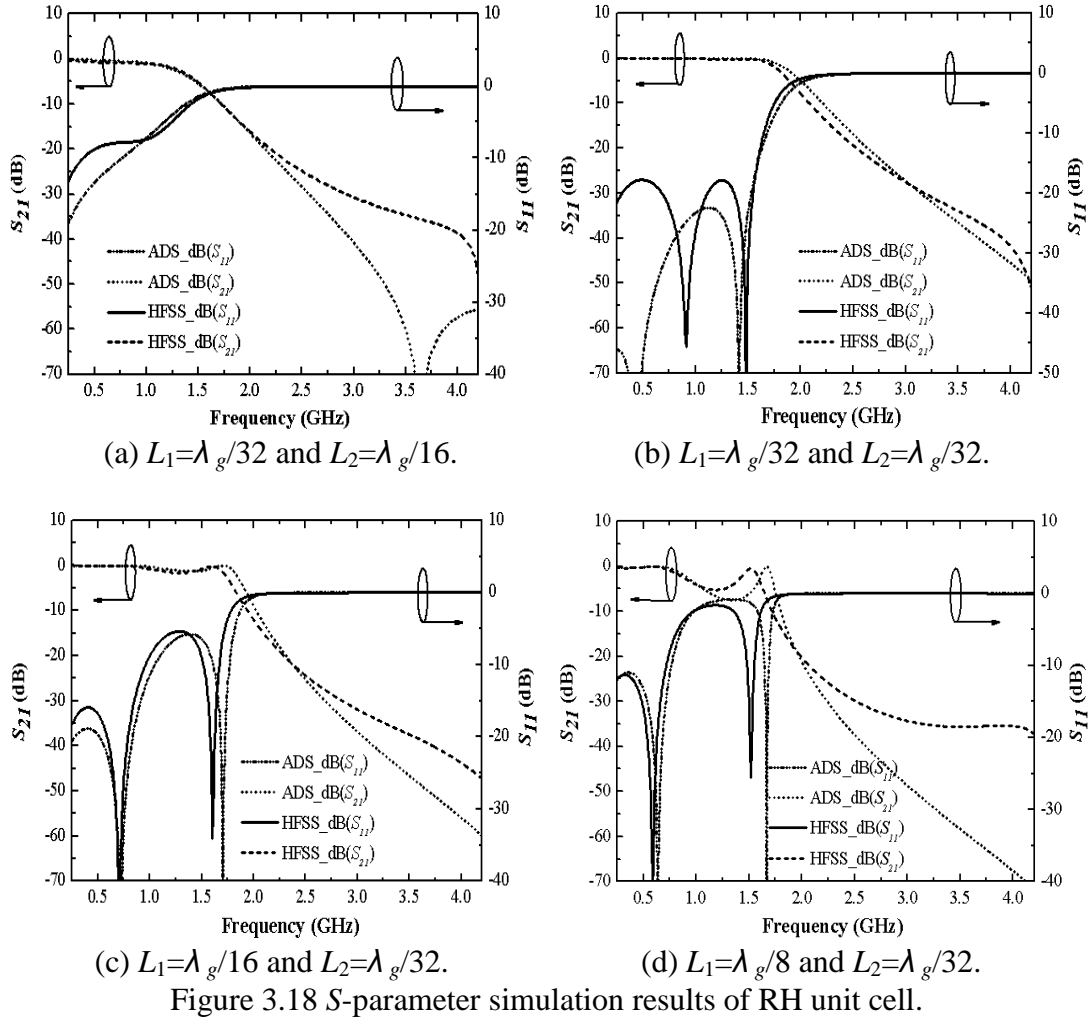Figure 3.17 Equivalent circuits for RH unit cell.

40

where L_s and L_p are distributed on the narrow signal lines and L_p controls the skirt effect of the RH unit cell in the stop-band. On the other hand, C_{p1} and C_{p3} are created between the broad signal lines and the bottom ground plane. And C_{p2} is created at the discontinuities of the signal lines with different widths [21]. But it has little effect on the characteristics since the value is small. Moreover, c is the velocity of light, ε_0 is the permittivity of free space, λ_g is the guided wavelength. And the values of the effective permittivity ε_{eff} and the characteristic impedance Z_c can be calculated responding to the signal line width and the gap width between the signal line and the side ground plane in CBCPW structure by the tool Linecalc in ADS.

3.2.2 Simulation Results of RH Unit Cell

The *S*-parameter simulation results of the RH unit cell and the equivalent circuit are plotted in Figure 3.18, which exhibits low-pass characteristics. Comparing the simulation results of the unit cell with the ones of the equivalent circuit, the graphs of *S* parameters exhibit similar forms and similar characteristics. As shown in Figure 3.18(a), the cutoff frequency of the RH unit cell is 1.37GHz and of the equivalent circuit is 1.33GHz. Therefore, the cutoff frequency error rate is 3.13%. Similarly, the error rates are calculated as 4.48%, 5.37% and 7.17% in Figure 3.18(b), (c) and (d), respectively. Comparing the lengths of the parameters, it is obvious that the error rate becomes larger when the length of the parameter L_1 approaches to $\lambda_g/8$. In other words, the electrical energy preserved between the broad signal line and the bottom ground plane is more than the calculated value when L_1 gets longer.

Comparing these four figures, the *S*-parameter characteristics are different. The magnitude of S_{21} curves in Figure 3.18(a) and (b) is the maximum flat in the pass-band, but gets ripples in the stop-band. Therefore, it can be seen as a quasi-elliptic filter [23]. On the other hand, the S_{21} curves in Figure 3.18(c) and (d) get ripples in both the pass-band and the stop-band, which are similar to the characteristics of an elliptic filter [23]. Overall, Figure 3.18(b) exhibits the best characteristics that the return loss is more than 17.78dB and the maximum magnitude of S_{21} is flat in the pass-band, while decreases monotonically in the stop-band. Compare the lengths of the parameters in Figure 3.18, the characteristics of the RH unit cell turn better when

41

the lengths of L_1, L_2 approach to $\lambda_g/32$. Since the lengths of LPF stubs are being $\lambda_g/8$ [24] or $\lambda_g/4$ [25] in general, the RH unit cell is more advantageous to achieve miniaturization in filter design.

(a) $L_1=\lambda_g/32$ and $L_2=\lambda_g/16$.

(b) $L_1=\lambda_g/32$ and $L_2=\lambda_g/32$.

(c) $L_1=\lambda_g/16$ and $L_2=\lambda_g/32$.

(d) $L_1=\lambda_g/8$ and $L_2=\lambda_g/32$.

Figure 3.18 S-parameter simulation results of RH unit cell.

The energy distribution of the electric field, corresponding to the accumulated energy distribution of the parallel circuit composition C_R, which is generated between the broad signal lines and the bottom ground plane, is shown in Figure 3.19(a). Because of the electromagnetic interaction, the electric energy turns to be the magnetic energy as time elapses. The energy distribution of the magnetic field, corresponding to the accumulated energy distribution of the series circuit component L_R, which is distributed on the narrow signal lines, is shown in Figure 3.19(b). This process is repeated while the signal energy transmits from the input port to the output port. Therefore, the transference and suppression of the input signal energy are achieved by the inductances and capacitances, which build up the RH unit cell. And according to the values of the inductances and capacitances, the RH unit cell shows the nature of a LPF. Eventually, the RH unit cell gets the characteristics of preserving the input electromagnetic energy and transmitting the energy to the output port without loss, as well as the characteristic of low-pass frequency selectivity.

3.2.3 Measurement Results of RH Unit Cell

The RH unit cell is fabricated with the physical dimensions shown in Table 3.8, and the layout pattern is shown in Figure 3.20. Then, the fabricated RH unit cell is measured and the *S*-parameter characteristics are plotted in Figure 3.21. It can be seen that a good agreement between the measurement and simulation results has been achieved. The measurement shows a 0.38dB insertion loss with -16dB suppression until 1.6GHz in the pass-band and a good skirt effect. Moreover, the maximum magnitude of the measured S_{21} curve decreases monotonically in the stop-band. As analyzed above, the RH unit cell can be used for LPF design.

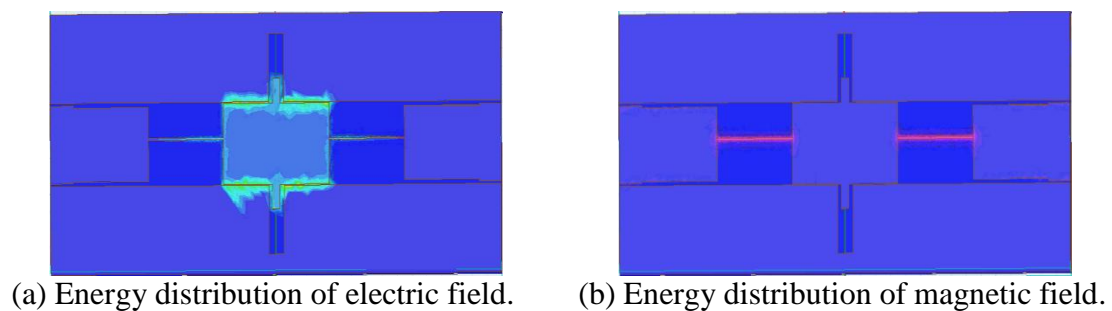(a) Energy distribution of electric field.　　(b) Energy distribution of magnetic field.
Figure 3.19 Energy distributions of RH unit cell.
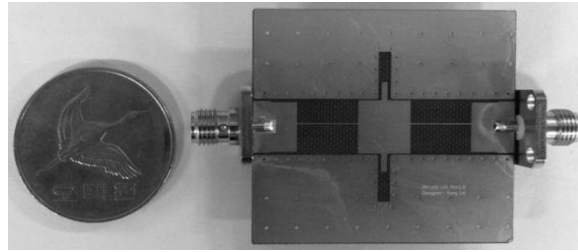
Figure 3.20 Fabricated RH unit cell.

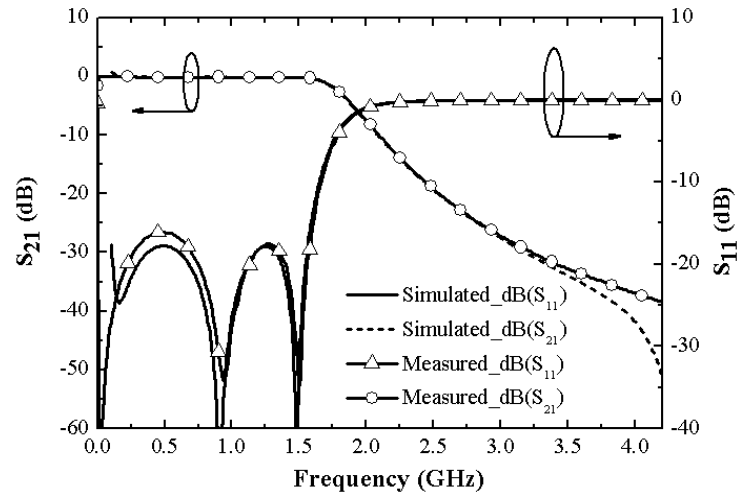Figure 3.21 *S*-parameter simulation and measurement results of RH unit cell.

Table 3.8 Physical dimensions of RH unit cell. (unit: mm)

Parameters	L_1	L_2	L_3	G_r	D	S_1	S_2	T	K	FE
Values	4.32	4.32	3	10	10	0.2	0.2	5	0.25	3

Chapter 4 Unit Cell Design Based on D-CRLH MTM TL

4.1 Unit Cell with Band-Rejection Property Based on D-CRLH CBCPW

4.1.1 CBDG Unit Cell Based on CBCPW

A unit cell is proposed based on D-CRLH CBCPW with a conductor-backed defected ground (CBDG) structure on the bottom layer, which is shown in Figure 4.1. The geometry consists of a dielectric substrate between two metallic layers and the signal line on the top layer is transformed into a U-shaped structure. In order to get band-rejection property, a U-shaped CBDG structure is etched on the bottom layer and one port of the CBDG structure is shorted to the bottom ground plane, the other is opened. Thus, the U-shaped signal line on the top layer and the U-shaped CBDG structure on the bottom layer make up a resonator. The characteristic impedance of the input and output ports is 50Ω, and the substrate thickness of 0.787mm and the relative dielectric constant ε_r of 2.5 is used for all cases.

As shown in Figure 4.1, the input port is symmetric with the output port on the top layer, based on the central axis of the U-shaped signal line. When the input signal transmits along the unit cell, the equivalent series LC parallel resonant circuit component L_R is distributed on the U-shaped signal line and the component C_L is generated in proportion to the coupling area of the resonator. On the other hand, the equivalent parallel LC series resonant circuit components L_L and C_R are created on the U-shaped CBDG structure. Since one port of the CBDG structure connects with the bottom ground plane, when the length of it is set to a quarter of the wavelength, the inductance L_L and the capacitance C_R can be generated at the same time. Therefore, the band-rejection resonance frequency can be moved to the desired frequency by adjusting the parameters W_0, CW_0, L_1, L_2, L_3 and S. In other words, the values of the components L_R, C_R, L_L, C_L in the equivalent circuit of Figure 4.2 change with the values of the parameters.

4.1.2 Simulation and Measurement Results of CBDG Unit Cell

The influences of the parameters L_1, L_3, W_0 and CW_0 are investigated and Figure 4.3 shows the simulated insertion loss characteristics done by HFSS. As L_1 increases

45

doubled and quadrupled, the resonant frequency decreases due to the series inductance of the series LC parallel resonant circuit L_R and the parallel LC series resonant circuit components L_L and C_R increase. And when L_3 increases, the values of the inductances L_L and L_R, and the capacitance C_R increase. Therefore, the resonant frequency decreases as L_3 increases. On the other hand, the resonant frequency decreases as W_0 increases, but increases as CW_0 increases. The reason is that the value of the inherent capacitances of the TL changes with the widths of the U-shaped signal line and the CBDG structure. And the interaction between the inherent capacitances effects different results.
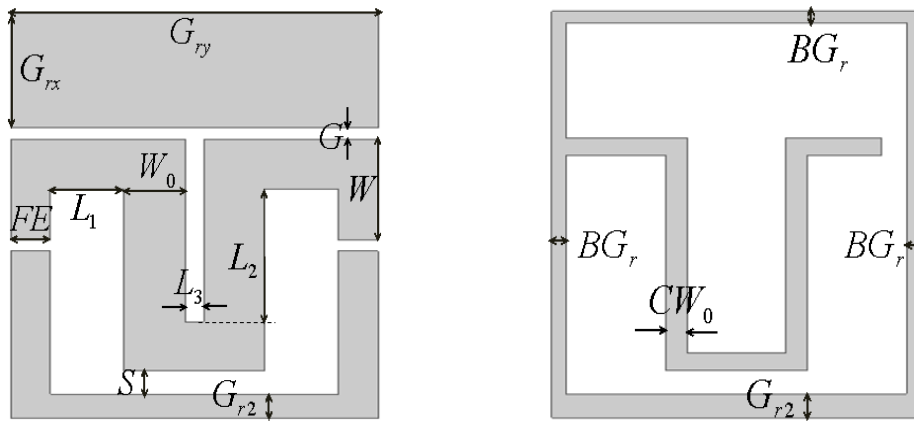
| (a) Top view. | (b) Bottom view. |

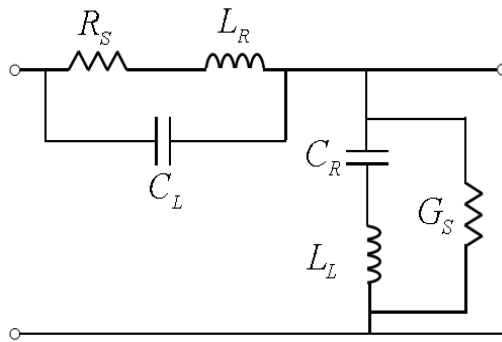Figure 4.1 Physical geometry of CBDG unit cell.

Figure 4.2 Equivalent circuit for CBDG unit cell.

The CBDG unit cell is fabricated with the physical dimensions shown in Table 4.1, which layout patterns are shown in Figure 4.4. Figure 4.5 shows the *S*-parameter simulation and measurement results. The fabricated CBDG unit cell exhibits good band-rejection characteristics as predicted by HFSS. The simulated resonant frequency of the CBDG unit cell is 885MHz and the measured resonant frequency is 883MHz. Therefore, the error rate of the resonant frequency is 0.23%. The measurement shows that the return loss is less than 0.6dB and the insertion loss is more than 16dB from 869 to 894MHz of the stop-band. And the insertion loss of pass-band at lower frequencies is less than 0.52dB and at higher frequencies is less than 1.34dB.

(a) L_1.   (b) L_3.
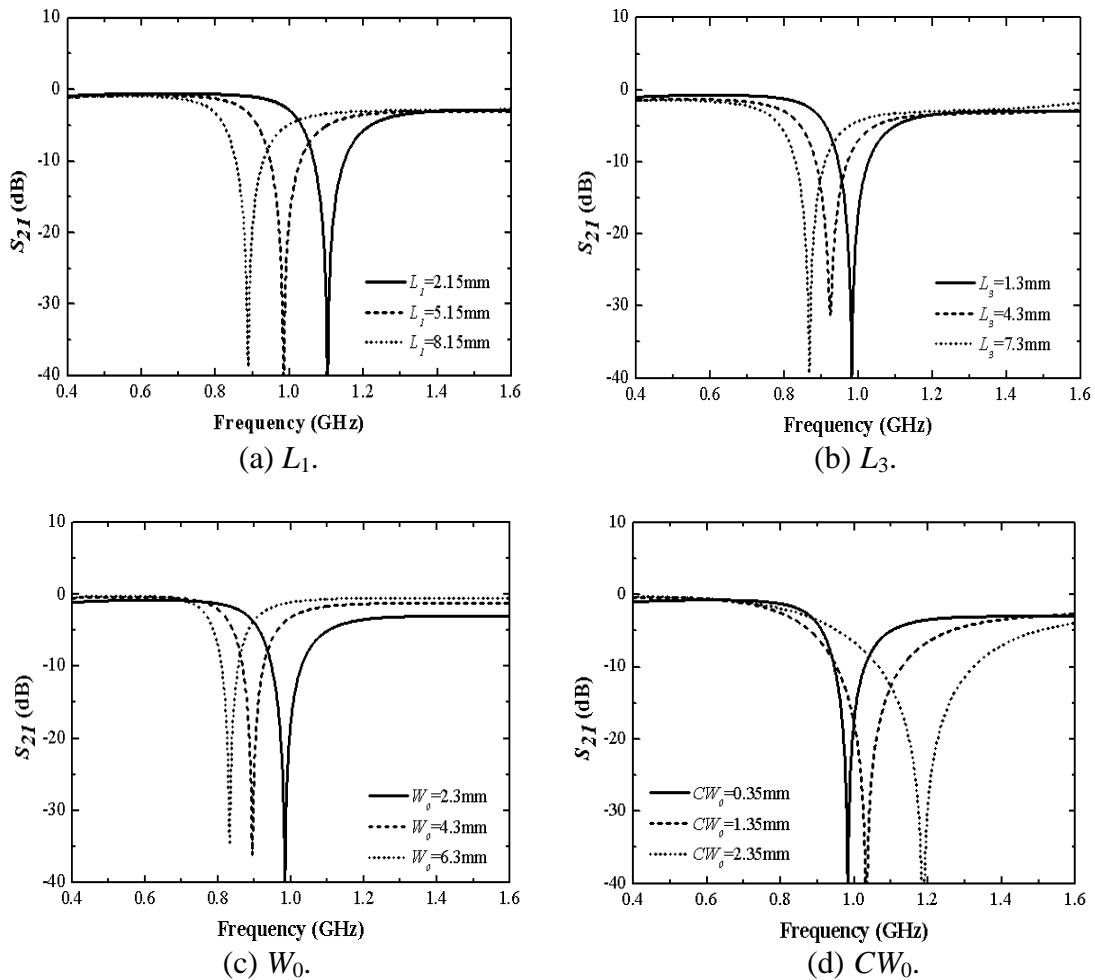
(c) W_0.   (d) CW_0.

Figure 4.3 Insertion loss characteristics as a function of geometrical parameters.

The dispersion characteristics to confirm the D-CRLH structure are shown in Figure 4.6. The propagation in the CBDG unit cell is forward at both low frequencies below the series resonant frequency of 850MHz and high frequencies above the shunt resonant frequency of 961MHz where the right-handed effect occurs. Otherwise, the propagation is backward between the series and shunt resonant frequencies, and left-handed effect occurs. Thus, the proposed CBDG unit cell exhibits the D-CRLH characteristics.
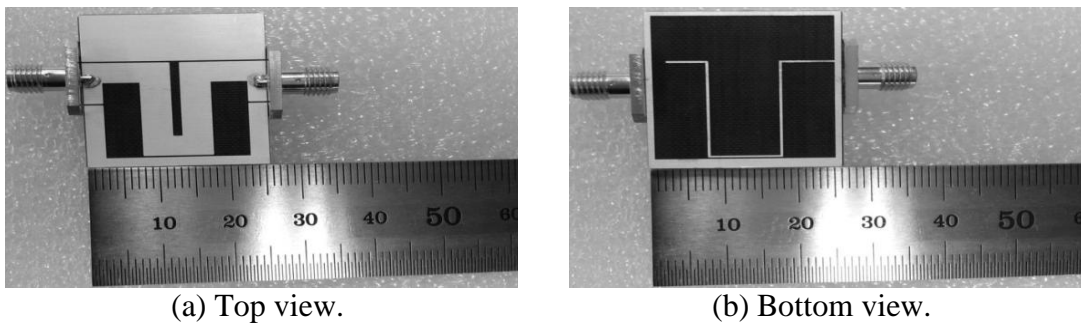

(a) Top view.   (b) Bottom view.
Figure 4.4 Fabricated CBDG unit cell.

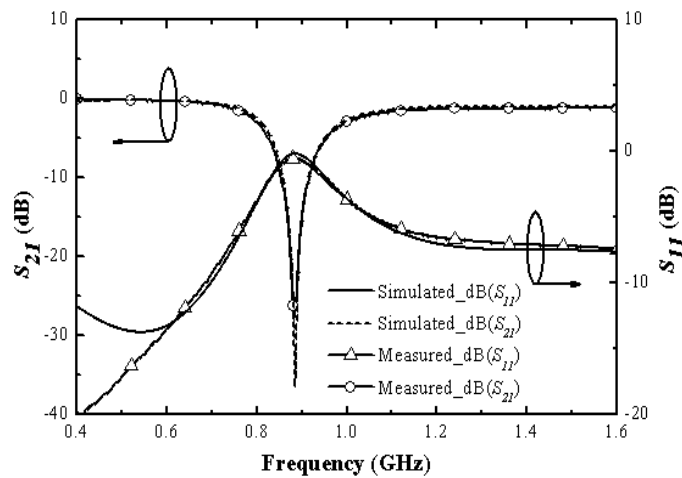Figure 4.5 *S*-parameter simulation and measurement results of CBDG unit cell.

Table 4.1 Physical dimensions of CBDG unit cell. (unit: mm)

Parameters	G_{rx}	G_{ry}	G	W	FE	W_0	L_1
Values	10	25.8	0.3	8.74	2.8	4.3	5.15
Parameters	L_2	L_3	S	G_{r2}	BG_r	CW_0	
Values	11.6	1.3	0.3	2.1	1	0.35	

The energy distribution of the electric field corresponds to the accumulated energy distribution of the capacitance C_L generated in the U-shaped resonator, and the capacitance C_R distributed on the U-shaped CBDG structure on the bottom layer. As shown in Figure 4.7(a), the energy generated more at the open port of the CBDG structure. As time elapses, the electric energy turns to be the magnetic energy. The energy distribution of the magnetic field corresponds to the accumulated energy distribution of the inductance L_L, which is also created on the CBDG structure. As shown in Figure 4.7(b), most of the magnetic energy accumulates at the short port of the CBDG structure. This process is repeated while the signal energy transmits from the input port to the output port. Therefore, the CBDG unit cell gets the characteristics of preserving the input electromagnetic energy and transmitting the energy to the output port without loss, as well as the characteristic of band-rejection frequency selectivity. As analyzed above, the proposed CBDG unit cell can be used for BRF design.
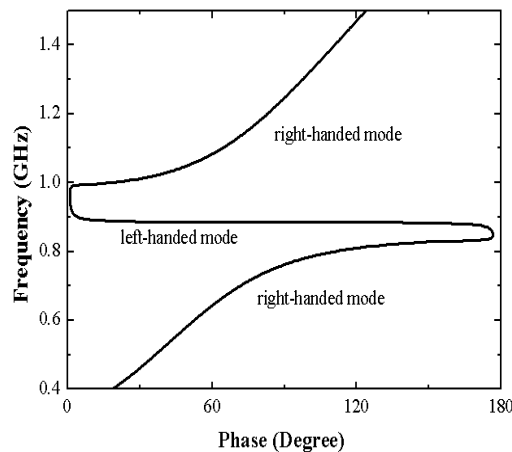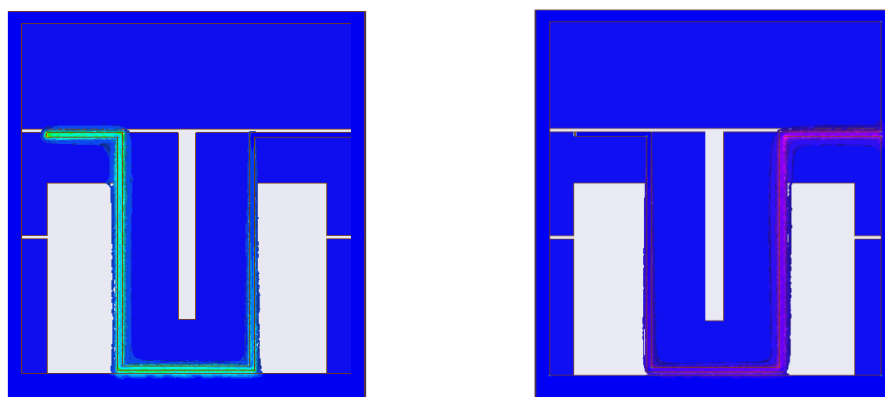

Figure 4.6 Dispersion characteristics of CBDG unit cell.

(a) Energy distribution of electric field.   (b) Energy distribution of magnetic field.
Figure 4.7 Energy distributions of CBDG unit cell.

제주대학교 중앙도서관
JEJU NATIONAL UNIVERSITY LIBRARY

4.2 Unit Cell with Band-Rejection Property Based on D-CRLH CPW

4.2.1 GL Unit Cell Based on CPW

The geometric configuration of the proposed unit cell based on D-CRLH CPW with a groove line (GL) structure is shown in Figure 4.8. In order to get band-rejection property and small size, a GL structure is etched on a side ground plane and one port is shorted to the side ground plane, the other is opened. Also, the signal line is transformed into a GL-like structure, which makes up a resonator with the GL structure. The characteristic impedance of the input and output ports is 50Ω, the substrate thickness H is 0.787mm and the relative dielectric constant ε_r is 2.5.

As shown in Figure 4.8, the input port is symmetric with the output port, based on the central axis of the groove signal line. But the groove resonator is not a symmetric structure because one port is open, the other is short. The equivalent circuit for the GL unit cell is shown in Figure 4.9. When the input signal transmits along the unit cell, the equivalent series LC parallel resonant circuit component L_R is distributed on the signal line. And the component C_L is generated in proportion to the coupling area of the resonator. On the other hand, the equivalent parallel LC series resonant circuit components L_L and C_R are created on the GL structure of the side ground plane. Since one port of the GL structure connects with the side ground plane, when the length of it is set to a quarter of the wavelength, the inductance L_L and the capacitance C_R can be generated at the same time.

4.2.2 Simulation and Measurement Results of GL Unit Cell

The influences of the parameters Y_2, Y_4, S_1 and X_c are investigated and Figure 4.10 shows the simulated insertion loss characteristics. As Y_2, Y_4 and X_c increase doubled and quadrupled, the resonant frequency decreases due to the capacitance of the series LC parallel resonant circuit C_L and the parallel LC series resonant circuit components L_L and C_R increase. And according as S_1 increases, the capacitance of the series LC parallel resonant circuit C_L decreases. Therefore, the resonant frequency increases as S_1 increases.
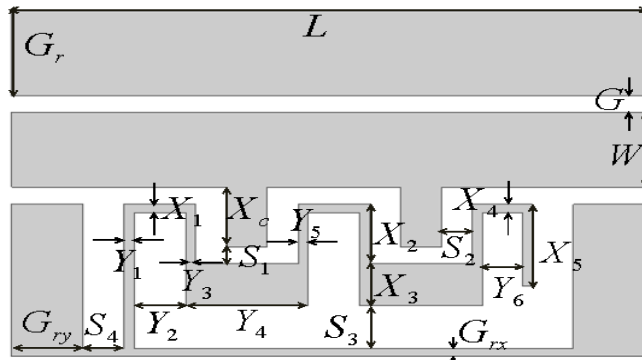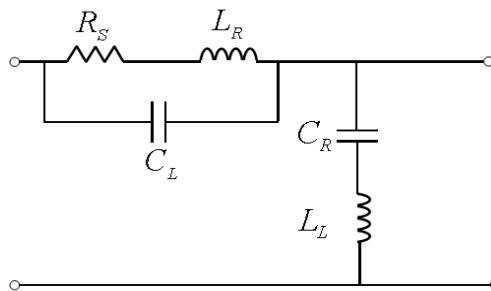
Figure 4.8 Physical geometry of GL unit cell.

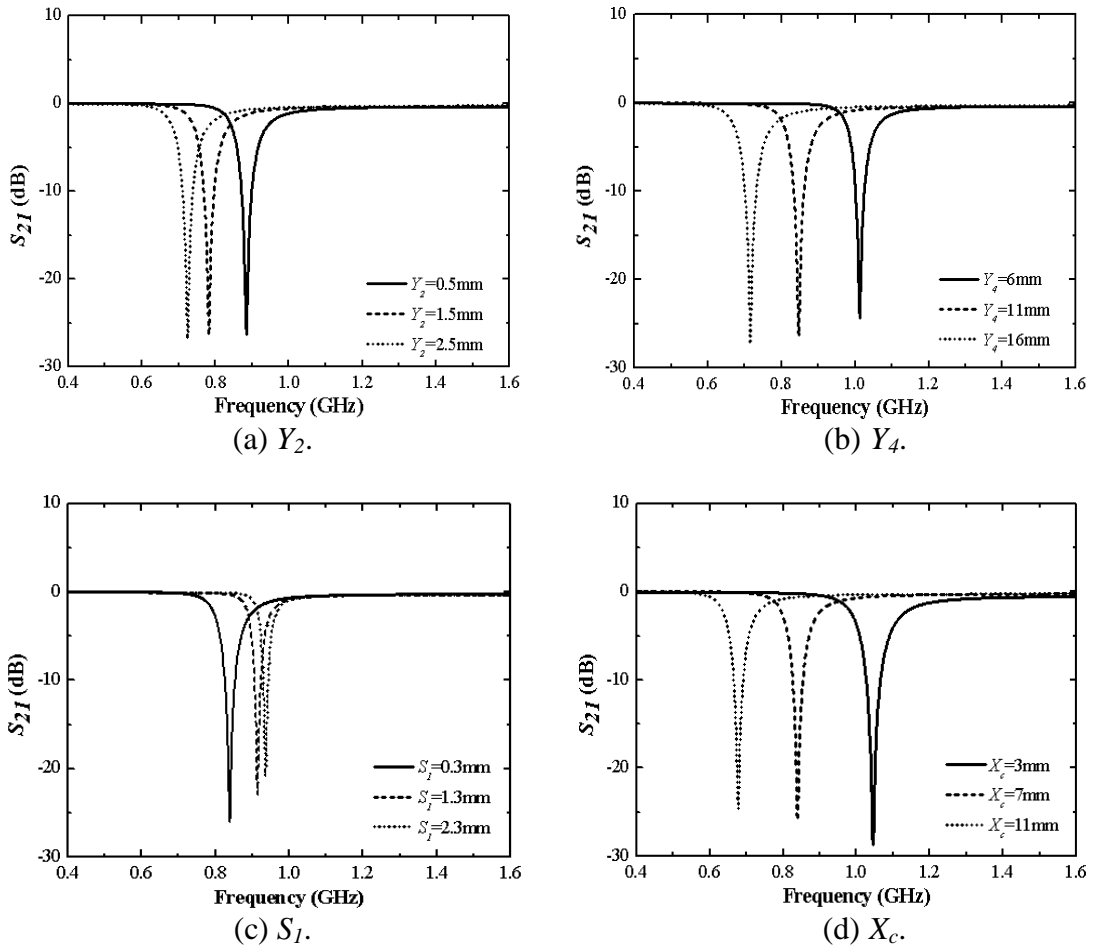
Figure 4.9 Equivalent circuit for GL unit cell.

(a) Y_2.

(b) Y_4.

(c) S_1.

(d) X_c.

Figure 4.10 Insertion loss characteristics as a function of geometrical parameters.

51

The GL unit cell is fabricated in the dimension of Table 4.2, as shown in Figure 4.11. And Figure 4.12 shows the comparison of *S*-parameter simulation and measurement results. The measurement shows a good agreement with the simulation results. The simulated resonant frequency is 881MHz and the measured result is 880MHz. Therefore, the error rate of the resonant frequency is only 0.11%. The measurement shows a 2dB return loss and an 11dB insertion loss from 869 to 894MHz of the stop-band. And the insertion loss of low frequency pass-band is less than 0.25dB and of high frequency pass-band is less than 0.98dB.
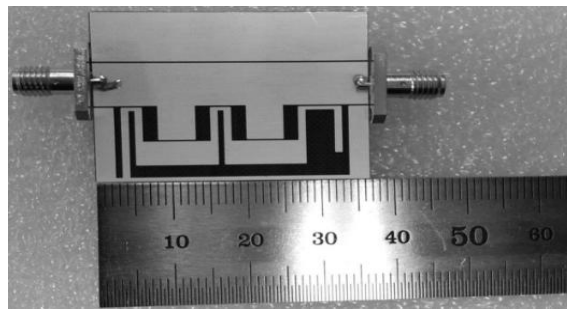
Figure 4.11 Fabricated GL unit cell.
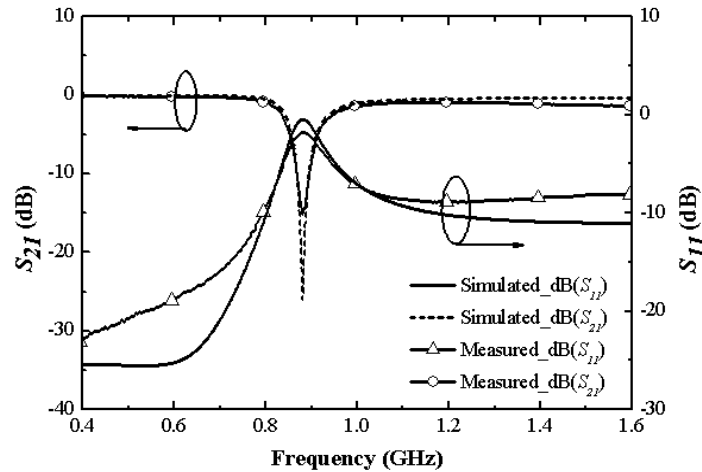
Figure 4.12 *S*-parameter simulation and measurement results of GL unit cell.

Table 4.2 Physical dimensions of GL unit cell. (unit: mm)

Parameters	G_r	L	G	W	G_{rx}	G_{ry}	X_1	X_2
Values	10	36.9	0.3	8.74	1	2.8	0.7	7
Parameters	X_3	X_4	X_5	X_c	Y_1	Y_2	Y_3	Y_4
Values	4.9	0.7	9.6	7	1	0.8	1	11
Parameters	Y_5	Y_6	S_1	S_2	S_3	S_4		
Values	1	3.9	0.3	2	2.5	0.9		

The dispersion characteristics of the GL unit cell are shown in Figure 4.13. The propagation is forward and the right-handed effect occurs at low frequencies below the series resonant frequency of 824MHz and at high frequencies above the shunt resonant frequency of 895MHz. Otherwise, the propagation is backward between the series and shunt resonant frequencies, and left-handed effect occurs. Thus, the proposed GL unit cell exhibits the D-CRLH characteristics.

The energy distribution of the electric field is shown in Figure 4.14(a), corresponding to the accumulated energy distribution of the capacitance C_L generated in proportion to the coupling area of the resonator, and the capacitance C_R distributed on the GL structure on the side ground plane. As time elapses, the electric energy turns to be the magnetic energy and the magnetic energy distribution corresponds to the accumulated energy distribution of the inductance L_L, which is also distributed on the GL ground structure. This process is repeated while the signal energy transmits from the input port to the output port. Eventually, the GL unit cell gets the characteristics of preserving the input electromagnetic energy and transmitting the energy to the output port without loss, as well as the characteristic of band-rejection frequency selectivity.
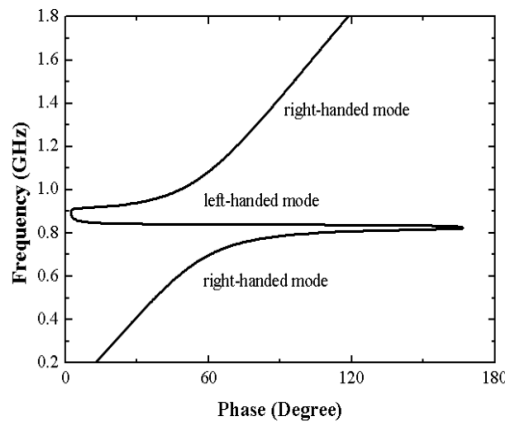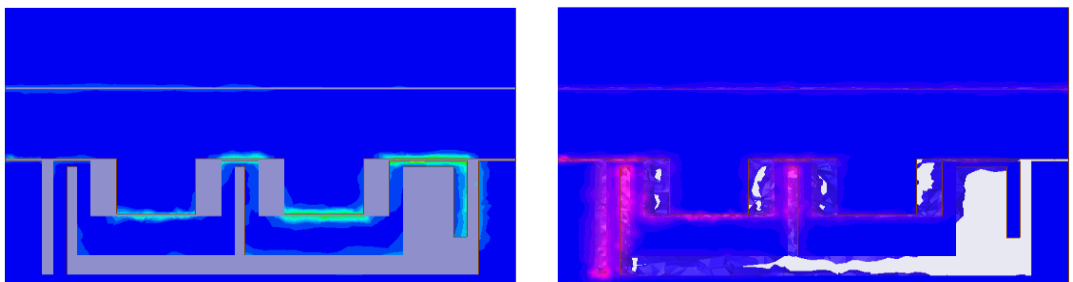

Figure 4.13 Dispersion characteristics of GL unit cell.

(a) Energy distribution of electric field. (b) Energy distribution of magnetic field.
Figure 4.14 Energy distributions of GL unit cell.

53

Chapter 5　Conclusions

This thesis focused on an analysis of the fundamental properties of MTMs and the unit cells with high-pass, low-pass and band-rejection property on CPW MTM TL. The equivalent circuits for the proposed unit cells were derived from the physical geometries and the characteristics of the unit cells. As a result, the equivalent circuits for the proposed unit cells showed good agreements with the proposed unit cells. And the dispersion characteristics and the energy distributions of the electromagnetic field were simulated to identify the C-CRLH and D-CRLH structures.

The LH unit cell based on C-CRLH FCPW showed high-pass property with -9.88dB suppression in the range beyond 2.05GHz. And the DLH unit cell based on C-CRLH FCPW exhibited high-pass property that the return loss is more than 10dB from 2.52GHz to 2.9GHz and beyond 4.23GHz of the pass-band. On the other hand, the RH unit cell based on C-CRLH CBCPW exhibited low-pass property with a 16dB return loss and a 0.38dB insertion loss in the pass-band.

The CBDG unit cell based on D-CRLH CBCPW with band-rejection property had a 0.6dB return loss and a 16dB insertion loss from 869MHz to 894MHz of the stop-band. Moreover, the GL unit cell based on D-CRLH CPW showed band-rejection property with a 2dB return loss and an 11dB insertion loss from 869MHz to 894MHz.

Since the proposed unit cells have good characteristics with small sizes, they can be used not only in filter design but also in other components of microwave systems, such as couplers and resonators. Especially, they are very useful for the dual-band or multi-band duplexers over operational frequencies separated and combined by various frequency bands. Contrary to conventional couplers, the unit cells based on MTM TL are good choices for coupler design by changing the DC offset and phase slope to intercept the desired phases at any arbitrary frequencies.

References

[1] V. Veselago, "The electrodynamics of substances with simultaneously negative values of ε and μ," *Soviet Physics Uspekhi*, vol. 10, no. 4, pp. 509-514, Feb. 1968.

[2] D. R. Smith, W. J. Padilla, D. C. Vier, S. C. Nemat-Nasser, and S. Schultz, "Composite medium with simultaneously negative permeability and permittivity," *Phys. Rev. Lett.*, vol. 84, no. 18, pp. 4184-4187, May 2000.

[3] C. Caloz and T. Itoh, "Application of the transmission line theory of left-handed (LH) materials to the realization of a microstrip LH transmission line," in *Proc. IEEE-AP-S USNC/URSI National Radio Science Meeting*, vol. 2, San Antonio, TX, June 2002, pp. 412-415.

[4] A. A. Oliner, "A planar negative-refractive-index medium without resonant elements," in *Proc. IEEE MTT-S International Symposium*, vol. 1, 2003, pp. 191-194.

[5] C. Caloz and T. Itoh, *Electromagnetic metamaterials: transmission line theory and microwave applications*, John Wiley & Sons, Inc., pp. 15, 83-84, 2006.

[6] A. Lai, T. Itoh, and C. Caloz, "Composite right/left-handed transmission line metamaterials," *IEEE Microw. Mag.*, pp. 34-50, Sept. 2004.

[7] C. Caloz and T. Itoh, "Novel microwave devices and structures based on the transmission line approach of meta-materials," in *Proc. IEEE MTT-S International Symposium*, vol. 1, June 2003, pp. 195-198.

[8] Qi Zhu and Shan-Jia Xu, "Composite right/left handed transmission line metamaterials and applications," in *Proc. Meta. 2008 International workshop*, Nov. 2008, pp. 72-75.

[9] J. Garcia-Garcia, I. B. Vendik, B. Sans, D. Kholodnyak, P. Kapitanova, J. Bonache, and F. Martin, "Miniaturization and optimization of planar microwave

filters based on metamaterials," in *Proc. Microwave Conf. 2007*, European, Oct. 2007, pp. 500-503.

[10] Rainee N. Simons, *Coplanar waveguide circuits, components, and systems*, John Wiley & Sons, Inc., pp. 1-3, 11-23, 87-109, 2001.

[11] Cheng P. Wen, "Coplanar waveguide: a surface strip transmission line suitable for nonreciprocal gyromagnetic device applications," *IEEE Trans. Microw. Theory Tech.*, vol. 17, no. 12, pp. 1087-1090, Dec. 1969.

[12] Giovanni Ghione and Carlo U. Naldi, "Coplanar waveguides for MMIC applications: effect of upper shielding, conductor backing, finite-extent ground planes, and line-to-line coupling," *IEEE Trans. Microw. Theory Tech.*, vol. 35, no. 3, pp. 260-267, Jan. 2003.

[13] M. E. Davis, E. W. Williams, and A. C. Celestini, "Finite-boundary corrections to the coplanar waveguide analysis," *IEEE Trans. Microwave Theory Tech.*, vol. 21, no. 9, pp. 594-596, Sept. 1973.

[14] Y. C. Shih and T. Itoh, "Analysis of conductor-backed coplanar waveguide," *Electron Lett.*, vol. 18, no. 12, pp. 538-540, Jun. 1982.

[15] C. Caloz, "Dual composite right/left-handed (D-CRLH) transmission line metamaterial," *IEEE Microw. Wireless Compon. Lett.*, vol. 16, no. 11, pp. 585-587, Nov. 2006.

[16] C. W. Chiu, "Inductance computation for coplanar waveguide discontinuities with finite metallization thickness," *IEE Proc., Microw. Antennas Propag.*, vol. 145, no.6, pp. 496-500, Dec. 1998.

[17] C. W. Chiu and R. B. Wu, "Capacitance computation for CPW discontinuities with finite metallization thickness by hybrid finite-element method," *IEEE Trans. Microw. Theory Tech.*, vol. 45, no. 4, pp. 498-504, April 1997.

[18] L. Yang, S. D. Seo, H. R. Cho, and D. Y. Yang, "Analysis of unit cells for filter design using CRLH transmission line," in *Proc. ICCE2012*, Aug. 2012, pp. 397-401.

[19] L. Yang, S. D. Seo, H. R. Cho, and D. Y. Yang, "Analysis of unit cells for high pass filter using left-handed transmission line," in *Proc. APCC2012*, Oct. 2012, pp. 29-33.

[20] L. Yang and D. Y. Yang, "Analysis and design of low pass filter using unit cell based on CRLH transmission line," *International Journal of Contents, Korea Contents Association*, vol. 8, no. 3, pp. 100-104, Sept. 2012.

[21] Jia-Sheng Hong, M. J. Lancaster, *Microstrip filters for RF/microwave applications,* John Wiley & Sons, Inc., pp. 97-99, 89-91, 2001.

[22] S. S. Bedair and I. Wolff, "Fast and accurate analytic formulas for calculating the parameters of a general broadside-coupled coplanar waveguide for (M)MIC applications," *IEEE Trans. Microw. Theory Tech.*, vol. 37, pp. 843-850, May 1989.

[23] D. Y. Kim, S. K. Choi, and C. H. Yoon, *Modern network synthesis theory and filter design*, Hongrueng Science Pub., pp. 77-82, 85-89, 1998.

[24] Kwangsik Park, Kwisoo Kim, Jongsik Lim, and Dal Ahn, "A new open stubs structure of Kuroda low-pass filter using DGS," in *Proc. WAMICON '09, IEEE 10th Annual*, Apr. 2009, pp. 1-4.

[25] Haojia Lin, Xiaoqun Chen, Xiaowei Shi, Lei Chen, and Yanfu Bai, "A wide stopband CPW low pass filter using quarter wavelength stepped impedance resonators," in *Proc. ICMMT Conf.*, May 2010, pp. 62-65.